

# The Boundary Conditions of the Heliosphere: Photoionization Models Constrained by Interstellar and *In Situ* Data

Jonathan D. Slavin<sup>1</sup> and Priscilla C. Frisch<sup>2</sup>

<sup>1</sup> Harvard-Smithsonian Center for Astrophysics, 60 Garden St., MS 83, Cambridge, MA 02138  
e-mail: jslavin@cfa.harvard.edu

<sup>2</sup> University of Chicago, Department of Astronomy and Astrophysics, 5640 S. Ellis Ave., Chicago, IL 60637  
e-mail: frisch@oddjob.uchicago.edu

Received – / Accepted –

## ABSTRACT

**Context.** The boundary conditions of the heliosphere are set by the ionization, density and composition of inflowing interstellar matter.

**Aims.** Constraining the properties of the Local Interstellar Cloud (LIC) at the heliosphere requires radiative transfer ionization models.

**Methods.** We model the background interstellar radiation field using observed stellar FUV and EUV emission and the diffuse soft X-ray background. We also model the emission from the boundary between the LIC and the hot Local Bubble (LB) plasma, assuming that the cloud is evaporating because of thermal conduction. We create a grid of models covering a plausible range of LIC and LB properties, and use the modeled radiation field as input to radiative transfer/thermal equilibrium calculations using the Cloudy code. Data from *in situ* observations of He<sup>0</sup>, pickup ions and anomalous cosmic rays in the heliosphere, and absorption line measurements towards  $\epsilon$  Cma were used to constrain the input parameters.

**Results.** A restricted range of assumed LIC H I column densities and LB plasma temperatures produce models that match all the observational constraints. The relative weakness of the constraints on  $N(\text{H I})$  and  $T_h$  contrast with the narrow limits predicted for the H<sup>0</sup> and electron density in the LIC at the Sun,  $n(\text{H}^0) = 0.19 - 0.20 \text{ cm}^{-3}$ , and  $n_e = 0.07 \pm 0.01 \text{ cm}^{-3}$ . Derived abundances are mostly typical for low density gas, with sub-solar Mg, Si and Fe, possibly subsolar O and N, and S about solar; however C is supersolar.

**Conclusions.** The interstellar gas at the Sun is warm, low density, and partially ionized, with  $n(\text{H}) \approx 0.23 - 0.27 \text{ cm}^{-3}$ ,  $T \approx 6300 \text{ K}$ ,  $X(\text{H}^+) \sim 0.2$ , and  $X(\text{He}^+) \sim 0.4$ . These results appear to be robust since acceptable models are found for substantially different input radiation fields. Our results favor low values for the reference solar abundances for the LIC composition.

**Key words.** ISM: clouds — ISM: abundances — ultraviolet: ISM — X-rays: diffuse background – solar system: general — ISM: cosmic rays

## 1. Introduction

The solar wind evacuates a cavity in the interstellar medium (ISM) known as the heliosphere, from which interstellar ions are excluded. In contrast, neutral interstellar gas flows through the heliosphere until destroyed by charge-transfer with the solar wind and photoionization. These neutrals form the parent population of pickup ions (PUI) and anomalous cosmic rays (ACR) observed inside of the heliosphere. The properties of the surrounding interstellar medium set the boundary conditions of the heliosphere and determine its configuration and evolution. An ionization gradient is expected in the cloud feeding ISM into the heliosphere because of the hardness of the interstellar radiation field and the low opacity of the ISM (Cheng & Bruhweiler 1990; Vallerga 1996; Slavin & Frisch 2002, hereafter SF02). Because of this ionization gradient, the densities of partially ionized species in the local interstellar cloud (LIC) will differ from the values in the circumheliosphere interstellar medium (CHISM) that forms the boundary conditions of the heliosphere. Hence we have undertaken a series of studies to determine the boundary conditions of the heliosphere based on both astronomical and heliospheric data. In turn our results provide tighter constraints on the heliosphere models used to calculate the filtration factors

for neutrals that then permit comparisons between ISM inside and outside of the heliosphere.

The distribution and velocity of interstellar H<sup>0</sup> inside of the heliosphere were first determined over 30 years ago from the fluorescence of solar Ly $\alpha$  radiation from these atoms (Thomas & Krassa 1971; Bertaux & Blamont 1971; Adams & Frisch 1977). Similar observations of solar 584Å fluorescence from interstellar He<sup>0</sup> showed that H/He  $\sim 6$  for interstellar gas inside of the heliosphere, in contrast to the cosmic value H/He = 10 (Ajello 1978; Weller & Meier 1981). More recent measurements of  $n(\text{H}^0)$  compared to  $n(\text{He}^0)$  inside of the heliosphere find a similar ratio of H/He  $\sim 6 - 7$  (Richardson et al. 2004; Gloeckler & Geiss 2004; Witte 2004; Möbius et al. 2004). This difference can be attributed to two effects: the loss of 40–60% of interstellar H<sup>0</sup> due to charge-transfer with protons in the heliosheath region, a process denoted “filtration” (Ripken & Fahr 1983), and the hardness of the interstellar radiation field at the Sun that ionizes more He than H (§4).

The *Copernicus* satellite first showed that the local interstellar cloud (LIC) surrounding the Sun is low density,  $\sim 0.1 \text{ atoms cm}^{-3}$ , partially ionized ( $n(\text{H}^+) \sim n(\text{H}^0)$ , York 1974; McClintock et al. 1975), and warm (temperature  $< 10^4 \text{ K}$ , e.g. McClintock et al. 1978). *Copernicus*, FUSE and HST data have shown that the cluster of local interstellar clouds (CLIC, low density clouds within  $\sim 30 \text{ pc}$ ), has low column densities,  $N(\text{H I}) < 10^{18.7}$ , and N ionization levels of  $> 30\%$  (e.g. Lehner et al.

2003; Wood et al. 2005), indicating partially ionized gas because H and N ionization are coupled by charge-transfer. The low column densities of the LIC itself,  $N(\text{H I}) < 10^{18} \text{ cm}^{-2}$ , indicate it is partially opaque to H ionizing radiation but not to He ionizing radiation. Cloud opacities of unity are reached for  $N(\text{H I}) \sim 10^{17.2} \text{ cm}^{-2}$  for photons close to the ionization threshold of hydrogen (13.6 eV), and  $N(\text{H I}) \sim 10^{17.7} \text{ cm}^{-2}$  for photons at the  $\text{He}^0$  ionization edge (24.6 eV). The result is that the LIC is partially ionized with a significant ionization gradient between the edge and center. Because of this radiative transfer effects are important and need to be modeled carefully in order to determine the boundary conditions of the heliosphere.

The LIC belongs to a flow of low density ISM embedded in the very low density and apparently hot ( $T \sim 10^6 \text{ K}$ ) Local Bubble (Frisch 1981; Frisch & York 1986; McCammon et al. 1983; Snowden et al. 1990). The bulk motion of the CLIC through the local standard of rest<sup>1</sup> corresponds to a velocity of  $-17.0$  to  $-19.4 \text{ km s}^{-1}$  from the direction  $\ell \sim 331^\circ$ ,  $b \sim -5^\circ$  (Frisch & Slavin 2006). This upwind direction is near the center of the Loop I superbubble and the center of the “ring” shadow that has been attributed to the merging of Loop I and the Local Bubble (Frisch & York 1986; Frisch 2007; Egger & Aschenbach 1995). Individual cloudlets with distinct velocities are identified in this flow (Lallement et al. 1986; Frisch et al. 2002). The velocity of the cloud feeding gas into the heliosphere has been determined by the velocity of interstellar  $\text{He}^0$  in the heliosphere measured by the GAS detector on Ulysses,  $-26.3 \text{ km s}^{-1}$  (Witte 2004).

Curiously, absorption lines at the LIC velocity are not observed in the nearest interstellar gas in the upwind hemisphere, such as towards the closest star  $\alpha \text{ Cen}$  or towards 36 Oph located  $\sim 5 \text{ pc}$  beyond the heliosphere nose (Adams & Frisch 1977; Landsman et al. 1984; Linsky & Wood 1996; Wood et al. 2000a,b). This lack of an absorption component at the LIC velocity in the closest stars in the upstream direction indicates that the Sun is near the edge of the LIC, so the CHISM may vary over short distances (and hence timescales).

We are able to test for possible past variations by comparing the first interplanetary  $\text{H}^0 \text{ Ly}\alpha$  glow spectrum obtained by *Copernicus* in 1975 with Hubble Space Telescope observations of the  $\text{Ly}\alpha$  spectra obtained during the mid-1990’s solar minimum conditions. The observed  $\text{H}^0$  velocity and intensity has not varied to within uncertainties over the twenty-year period separating these two sets of observations, so that the CHISM velocity field is relatively smooth over spatial scales of  $\sim 120 \text{ AU}$  in the downwind direction (Frisch & Slavin 2005). The 1975 *Copernicus* data were acquired in the direction corresponding to ecliptic longitudes of  $\lambda = 264.3^\circ$ ,  $\beta = +15.0^\circ$ , or  $\sim 13.3^\circ$  from the most recent upwind direction derived from SOHO H I  $\text{Ly}\alpha$  data (Qu  merais et al. 2006b,a, Q06). The *Copernicus* look direction was just outside of the “groove” expected in the  $\text{Ly}\alpha$  glow in the ecliptic during solar minimum. The groove is caused by increased charge-transfer in the solar wind current sheet, which has a small tilt during minimum conditions (Bzowski 2003). The velocity of the  $\text{Ly}\alpha$  profile observed by *Copernicus* corresponds to  $-24.8 \pm 2.6 \text{ km s}^{-1}$ , after correction to the SOHO upwind direction. Since Q06 measured  $\text{H}^0$  upwind velocities during the solar minimum years of 1996 and 1997 of  $-25.7 \pm 0.2 \text{ km s}^{-1}$  and  $-25.3 \pm 0.2 \text{ km s}^{-1}$ , which is consistent with the *Copernicus* results, we must arrive at the conclusion that the flow of interstellar  $\text{H}^0$  into the heliosphere was relatively constant be-

tween the years of 1975 and 1997, so that any observations of variations in the interplanetary  $\text{Ly}\alpha$  glow properties must be due to solar activity properties alone. The thermal broadening of the *Copernicus* spectrum corresponded to a temperature of  $\sim 5400 \text{ K}$ , however measurement uncertainties allowed temperatures of up to  $20,000 \text{ K}$ .

In this paper we present new photoionization models of the LIC and show they reproduce both the densities of the ISM at the heliosphere and column densities in the LIC component towards the star  $\epsilon \text{ CMa}$ . In earlier papers, photoionization models of both the “LIC” and “Blue Cloud” components observed towards  $\epsilon \text{ CMa}$  were used to constrain the models (SF02, Frisch & Slavin 2003). SF02 grouped the properties of the LIC and Blue Cloud, both of which are with  $2.7 \text{ pc}$  of the Sun because they are also observed towards Sirius,  $\sim 12^\circ$  from the  $\epsilon \text{ CMa}$  sightline. The LIC velocity and density are sampled by observations of interstellar  $\text{He I}$  inside of the heliosphere ( $-26.3 \text{ km s}^{-1}$ , Witte 2004), and Gry & Jenkins (2001) show that the properties of the LIC and Blue Cloud differ somewhat. The present study therefore focuses on obtaining the best model of heliosphere boundary conditions by using only data on the LIC inside of the heliosphere, and the LIC component towards  $\epsilon \text{ CMa}$ . The present study also benefits from new atomic rates for the critical  $\text{Mg II} \rightarrow \text{Mg I}$  dielectronic recombination coefficient, improved cooling rates in the radiative transfer code Cloudy, recent values for the pickup ion densities at the termination shock, and recent values for solar abundances.

The most truly unique quality of the LIC is that we are inside of it and therefore have the ability to sample the cloud directly via *in situ* observations carried out by a variety of spacecraft within the Solar System. Of all the available measurements of LIC gas flowing into the Solar System, the observations of the density and temperature of neutral He are apparently the most robust. Helium, unlike hydrogen, undergoes little ionization or heating in traversing the heliosheath regions, no deflection due to radiation pressure, and is destroyed by photoionization and electron-impact ionization within  $\sim 1 \text{ AU}$  of the Sun, so we expect that the density and temperature of  $\text{He}^0$  derived from the observations in the Solar System are truly representative of the values in the LIC (M  bius et al. 2004). In this paper we put a special emphasis on matching these  $\text{He I}$  data by determining model parameters that yield close agreement with the  $n(\text{He}^0)$  and  $T(\text{He}^0)$  data simultaneously.

## 2. Photoionization Model Constraints and Assumptions

The primary data constraints on our photoionization models are the LIC component column densities towards  $\epsilon \text{ CMa}$ , (Gry & Jenkins 2001, hereafter GJ01), *in situ* observations of  $\text{He}^0$  (Witte 2004; M  bius et al. 2004), pickup ions (PUI, Gloeckler & Fisk 2007), and anomalous cosmic rays (ACR, Cummings et al. 2002). The astronomical and *in situ* observational constraints are summarized in Table 1.

### 2.1. Astronomical Constraints – The LIC towards $\epsilon \text{ CMa}$

The data toward  $\epsilon \text{ CMa}$  of GJ01 show four separate velocity components detected in several different ions including C II, Si II, and Mg II. One of these velocity components, with a heliocentric velocity of  $\sim 17 \text{ km s}^{-1}$ , is identified as the LIC. Another is identified with a second local cloud, the “Blue Cloud” (BC) at  $\sim 10 \text{ km s}^{-1}$ . In our previous study of LIC ioniza-

<sup>1</sup> Heliocentric motions are converted to the local standard of rest, LSR, using the Standard solar apex motion.

**Table 1.** Observational Constraints

Observed Quantity	Observed <sup>a</sup> Value	Notes <sup>b</sup>
$N(\text{C II})$ ( $\text{cm}^{-2}$ )	$1.4 - 2.1 \times 10^{14}$	1, S
$N(\text{C II}^*)$ ( $\text{cm}^{-2}$ )	$1.3 \pm 0.2 \times 10^{12}$	1
$N(\text{C IV})$ ( $\text{cm}^{-2}$ )	$1.2 \pm 0.3 \times 10^{12}$	1
$N(\text{N I})$ ( $\text{cm}^{-2}$ )	$1.70 \pm 0.05 \times 10^{13}$	1
$N(\text{O I})$ ( $\text{cm}^{-2}$ )	$1.4_{-0.2}^{+0.5} \times 10^{14}$	1, S
$N(\text{Mg I})$ ( $\text{cm}^{-2}$ )	$7 \pm 2 \times 10^9$	1
$N(\text{Mg II})$ ( $\text{cm}^{-2}$ )	$3.1 \pm 0.1 \times 10^{12}$	1
$N(\text{Si II})$ ( $\text{cm}^{-2}$ )	$4.52 \pm 0.2 \times 10^{12}$	1
$N(\text{Si III})$ ( $\text{cm}^{-2}$ )	$2.3 \pm 0.2 \times 10^{12}$	1
$N(\text{S II})$ ( $\text{cm}^{-2}$ )	$8.6 \pm 2.1 \times 10^{12}$	1
$N(\text{Fe II})$ ( $\text{cm}^{-2}$ )	$1.35 \pm 0.05 \times 10^{12}$	1
$N(\text{H I})/N(\text{He I})$	$14 \pm 0.4^c$	2
$T$ (K)	$6300 \pm 340$	4
$n(\text{He}^0)$ ( $\text{cm}^{-3}$ )	$0.015 \pm 0.003$	4, $f = 1^d$
$n(\text{N}^0)^e$ ( $\text{cm}^{-3}$ )	$5.47 \pm 1.37 \times 10^{-6}$	3, $f = 0.68 - 0.95^d$
$n(\text{O}^0)^e$ ( $\text{cm}^{-3}$ )	$4.82 \pm 0.53 \times 10^{-5}$	3, $f = 0.64 - 0.99^d$
$n(\text{Ne}^0)^e$ ( $\text{cm}^{-3}$ )	$5.82 \pm 1.16 \times 10^{-6}$	3, $f = 0.84 - 0.95^d$
$n(\text{Ar}^0)^e$ ( $\text{cm}^{-3}$ )	$1.63 \pm 0.73 \times 10^{-7}$	3, $f = 0.53 - 0.95^d$

<sup>a</sup>  $N(\text{C II}^*)$ ,  $N(\text{N I})$ ,  $N(\text{O I})$ ,  $N(\text{Mg II})$ ,  $N(\text{Si II})$ ,  $N(\text{S II})$  and  $N(\text{Fe II})$  are used to constrain the input abundances of the models.

<sup>b</sup> The first number indicates the reference (below), and ‘‘S’’ indicates that the column density is based on a saturated line. Filtration factors ( $f$ , §2.2) are listed for neutrals that have been observed as pickup ions.

<sup>c</sup> The uncertainty given is only that due to uncertainties listed in Dupuis et al. (1995) for the observed  $\text{H I}$  and  $\text{He I}$  column densities with the implicit assumption that the ratio is the same on all lines of sight. Given the substantial intrinsic variation in this ratio, however, the quoted uncertainty must be regarded as a lower limit to the true uncertainty.

<sup>d</sup> We assume in this paper that for  $\text{He } f_{\text{He}} = 1$ , and  $f$  is not allowed to exceed 1. Heliosphere models predict the range  $f_{\text{He}} = 0.92 - 1$  for  $\text{He}$  and  $f_{\text{H}} = 0.50 - 0.74$  for  $\text{H}$  (see filtration factors in Cummings et al. 2002; Müller & Zank 2004a; Müller et al. 2007; Izmodenov et al. 2004).

<sup>e</sup> Note that the pickup ion ratios are for values at the termination shock.  $\text{N}^0$ ,  $\text{O}^0$ ,  $\text{Ne}^0$ , and  $\text{Ar}^0$  densities need to be corrected for filtration in the heliosheath regions (2.2).

References: (1) Gry & Jenkins (2001) Note that the values shown are for the LIC component towards  $\epsilon$  CMa.; (2) Dupuis et al. (1995); (3) Gloeckler & Fisk (2007); (4) Witte (2004).

tion (SF02) we noted that since the BC is close to the LIC, and both are detected towards Sirius at 2.7 pc (Lallement et al. 1994; Hébrard et al. 1999), perhaps actually abutting the LIC, we should treat the two as a single cloud for this line of sight. Counter arguments to this line of reasoning include the fact that the BC apparently has different properties than the LIC, though whether it is colder or hotter is unclear (see Hébrard et al. 1999, GJ01). For this reason and because we wish to find the ionization models that best predict interstellar neutral densities inside and outside of the heliosphere, we assume in this paper that the LIC and BC are truly separate clouds and select only the LIC components towards  $\epsilon$  CMa to constrain the models.

In the context of these models, the best astronomical constraints on the neutral ISM component are  $\text{N I}$ , the saturated  $\text{O I}$  line, and to some extent  $\text{Mg I}$  (though the line is weak). The electron density can be deduced from the ratio  $\text{Mg II}/\text{Mg I}$ , which is determined by photoionization and both dielectronic and radiative recombination, and the excitation of the  $\text{C II}$  fine-structure lines,  $\text{C II}/\text{C II}^*$ . However, the heavy saturation of the  $\text{C II}$  1335

Å line in the ISM limits the accuracy of the determination of  $N(\text{C II})$ , so in this paper we have de-emphasized  $\text{C II}/\text{C II}^*$  as an ionization diagnostic. For a discussion of the use of  $\text{C II}/\text{C II}^*$  and other observations in diagnosing the C abundance and C/S ratio see Slavin & Frisch (2006). Elements with first ionization potentials (FIP) < 13.6 eV (e.g. Mg, Si, S, and Fe) are generally almost entirely singly ionized in the LIC and thus the column densities of these ions are close to the total column densities for the elements.

## 2.2. In situ Constraints – $\text{He}^0$ , Pickup Ions, and Anomalous Cosmic Rays

Neutral atoms in the LIC penetrate the outer heliosphere regions, and become ionized primarily by charge-transfer with the solar wind ions, photoionization, and electron impact ionization (Rucinski et al. 1996). The composition of this neutral population reflects the partially ionized state of the LIC, rather than indicating a pure FIP effect. Thus the observed abundances of neutrals representing high FIP elements, such as He, Ne, and Ar, as well as H, N, and O, do not reflect their elemental abundances directly. As a result, these neutrals provide an interesting and unique constraint on the photoionization models. Once ionized, these interstellar wind particles form a population of ions with a distinct velocity distribution that are ‘‘picked up’’ by the solar wind and convected outwards, where they are measured by various spacecraft (Möbius et al. 2004; Gloeckler & Geiss 2004). These pickup ions (PUI) are accelerated in the heliosheath region and form a population of cosmic rays with an anomalous composition reflective of their origin as interstellar neutrals in a partially ionized gas (Cummings et al. 2002). *In situ* observations of these byproducts of the ISM interaction with the heliosphere, H, He, N, O, Ar, and Ne, provide a unique opportunity to constrain theoretical models of an interstellar cloud using the combination of sightline-integrated data, and data from a ‘‘single’’ spatial location, the heliosphere.

We adopt the Ulysses He measurements as the best set of constraints on the ISM inside of the heliosphere. The Ulysses satellite provides direct measurements of interstellar  $\text{He}^0$  at high ecliptic latitudes throughout the solar cycle (the GAS detector, Witte 2004) and also measurements of the He pickup ion component (the SWICS detector Gloeckler & Geiss 2004; Gloeckler & Geiss 2007). Although interstellar  $\text{He}^0$  close to the Sun is detected through the resonant scattering of solar 584 Å radiation, geocoronal contamination of the interstellar signal is present so we prefer the Ulysses data (Möbius et al. 2004). We adopt the Ulysses GAS and SWICS results,  $n(\text{He}^0) = 0.0151 \pm 0.0015 \text{ cm}^{-3}$ ,  $T(\text{He}^0) = 6,300 \pm 340 \text{ K}$ .

Data on the density of neutral N, O, Ne, and Ar in the surrounding ISM are provided by PUI and ACR data. The densities of interstellar  $\text{N}^0$ ,  $\text{O}^0$ ,  $\text{Ne}^0$ , and  $\text{Ar}^0$  at the termination shock are listed in Table 1. These densities must be corrected by the filtration factors, which correspond to the ratios of the densities at the termination shock to those in the LIC. Filtration occurs when neutral interstellar atoms are removed from the inflow by charge-transfer with interstellar protons as the atom crosses the heliosheath regions. Filtration values are listed in Table 1, based on values in Cummings et al. (2002); Müller & Zank (2004b); Izmodenov et al. (2004). Filtration values larger than 1 are not considered, although some models suggest possible net creation of  $\text{O}^0$  through charge-transfer between  $\text{O}^+$  and  $\text{H}^0$  in the heliosheath regions (Müller & Zank 2004a). We adopt  $f_{\text{He}} = 1$  for He. Our models must be compared to the interstellar densities

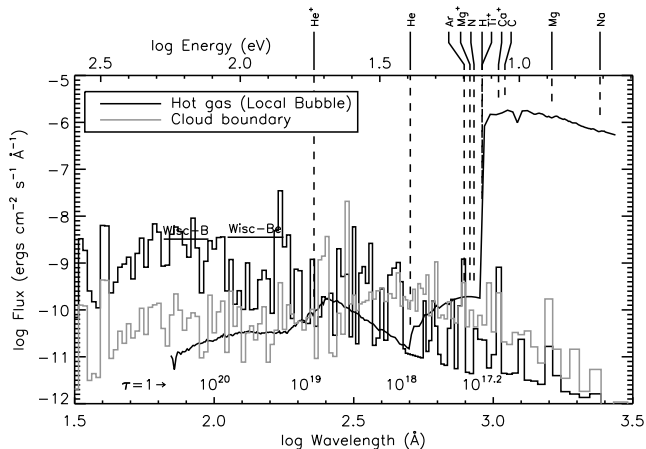


**Fig. 1.** The modeled interstellar radiation field at the Sun (model 26) is shown as a function of wavelength (bottom X-axis) and energy (top X-axis). The black histogram is the modeled hot gas (i.e. Local Bubble) spectrum while the gray histogram is the cloud boundary contribution. The other line is the stellar EUV/FUV background. The list of elements at the top of the plot identifies the ionization potentials for neutrals and ions of interest. The energy/wavelength at which an optical depth of 1 is reached for several different H I column densities is shown along the bottom of the plot. Observed flux levels of the soft X-ray diffuse background in the Wisconsin Be and B bands are plotted as lines (Bloch et al. 1986; McCammon et al. 1983).

obtained by correcting densities at the termination shock by filtration factors.

### 2.3. Interstellar Radiation Field at the Cloud Surface

The spectrum and flux of the cosmic radiation field control the ionization of the very local warm partially ionized medium (WPIM). The local interstellar radiation field (ISRF) that ionizes the LIC and other nearby cloudlets is determined by the location of the Sun in the interior of a hole in the neutral interstellar gas and dust and referred to as the Local Bubble. The clustering tendency of hot O and B stars, and attenuation of radiation by interstellar dust and gas, yield the well known spatial variation of the intensity and spectrum of the ISRF. We ignore possible temporal variations of the radiation field (e.g. Parravano et al. 2003), and model the ISRF throughout the LIC based on the observations of the present-day radiation field.

The radiation field we use in our models is based on observations of the ISRF at the Sun, supplemented by theoretical calculations of the spectra in the EUV and soft X-rays where lack of sensitivity and/or spectral resolution require the use of models to create a realistic spectrum. The directly observed radiation field includes the far ultraviolet (FUV) field created primarily by B stars, the extreme ultraviolet (EUV) field from two B stars ( $\epsilon$  CMA and  $\beta$  CMA) and hot nearby white-dwarf stars, and the diffuse soft X-ray background (SXR). We show the radiation field at the cloud surface in Fig. 1. Because the interstellar opacity for radiation with  $E > 13.6$  eV is vastly greater than for  $E < 13.6$  eV, the EUV part of the ISRF originates in nearby regions with  $N(\text{H I}) \lesssim 10^{18} \text{ cm}^{-2}$  while the FUV comes from a much larger volume.

We use the EUV field of Vallerga (1998), which is based on data collected by the Extreme Ultraviolet Explorer (EUVE)

satellite. The EUVE spectrometers were sensitive over the wavelength range of 504 – 730 Å and showed that the stellar part of the EUV background is dominated by  $\epsilon$  CMA and  $\beta$  CMA with substantial contributions from nearby hot white dwarfs at shorter wavelengths. Vallerga extrapolated those measurements to the H<sup>0</sup> ionization edge at 912 Å using a total interstellar H<sup>0</sup> density towards  $\epsilon$  CMA of  $N(\text{H I}) = 9 \times 10^{17} \text{ cm}^{-2}$ . This value for  $N(\text{H I})$  appears somewhat high based on observations of Gry & Jenkins (2001) which, though dependent on assumptions for gas phase abundances, indicate a value for  $N(\text{H I})$  of  $\sim 7 \times 10^{17} \text{ cm}^{-2}$ . This uncertainty in the total  $N(\text{H I})$  affects only the extrapolated portion of the spectrum in our models since the other portion of the spectrum is derived by de-absorbing the observed spectrum by the value of  $N(\text{H I})$  assumed just for the LIC. For the results presented here we have assumed that the total  $N(\text{H I})$  towards  $\epsilon$  CMA is  $7 \times 10^{17} \text{ cm}^{-2}$ . Assuming a larger value would increase the flux in the extrapolated region, though our calculations indicate that the overall affect on our results is only at the  $\sim 2\%$  level at most.

The FUV field is important because it sets the ionization rate of Mg<sup>0</sup>, which has a first ionization potential of 7.65 eV (1621 Å). The radiation field shortwards of 1600 Å is heavily dominated by O and B stars in Gould’s Belt, particularly those occupying the unattenuated regions of the third and fourth galactic quadrants. A pronounced spatial asymmetry in the 1565 Å radiation field has been observed by the TD-1 satellite S2/68 telescope survey of the interstellar radiation field, and we use those data and the extrapolation down to 912 Å from the 1564 Å measurements as calculated by Gondhalekar et al. (1980). The asymmetries in the TD-1 1565 Å radiation field are reproduced by diffuse interstellar radiation field models (Henry 2002).

The diffuse soft X-ray background (SXR) has been observed over the entire sky at relatively low spatial and spectral resolution by *ROSAT* (Snowden et al. 1997) and proportional counters flown on sounding rockets by the Wisconsin group (e.g., McCammon et al. 1983). The broadband count rates in the low energy bands, particularly the B and C bands (130–188 eV and 160–284 eV respectively) have been modeled as coming from an optically thin, hot plasma at a temperature of  $\sim 10^6$  K that occupies the low density cavity extending to  $\sim 50$ –200 pc from the Sun in all directions (Snowden et al. 1990). Refinements to this picture have been required by *ROSAT* data showing absorption by relatively distant clouds (e.g. MBM12, Snowden et al. 1993). Snowden et al. (1998) propose a picture in which the emission is divided between a LB component (unabsorbed except for the LIC) and a distant absorbed component, mainly in the Galactic halo. More recently there has been growing evidence that some, possibly large, fraction of the SXR is generated within the heliosphere from charge exchange between solar wind ions and neutral atoms (SWCX). We discuss this further in §5.6.

We model the spectrum measured by the broad-band soft X-ray observations by assuming that the SXR background consists of a local (unabsorbed) component and a distant (halo) component absorbed by an H I column density of  $10^{19} \text{ cm}^{-2}$ . The emission measure or intrinsic intensity of the local and distant components are assumed to be equal. The spectrum is calculated using the Raymond & Smith (1977, updated) plasma emission code assuming a hot, optically thin plasma in collisional ionization equilibrium. We explore temperatures for the hot gas of  $\log T_h = 5.9, 6.0$  and  $6.1$ . The total flux, scaled by the emission measure, is fixed so that the B band flux matches the all-sky average from McCammon et al. (1983).

The boundary region between the warm LIC and the adjacent Local Bubble plasma may be another significant source of EUV radiation and we include this flux in our models 1–30. We model this transition region as a conductive interface between the LIC and Local Bubble plasma in the same way as described in Slavin & Frisch (2002). The cloud is assumed to be steadily evaporating into the surrounding hot gas. The partially ionized gas of the LIC is heated and ionized as it flows into the Local Bubble. The ionization falls out of equilibrium, with low ionization stages persisting into the hot gas. The non-equilibrium ionization is followed and the emission in the boundary is calculated again using the Raymond & Smith (1977) code. Ions in the outflow are typically excited several times before being ionized and the boundary region radiates strongly in the 13.6 – 54.4 eV band. The contribution of the interface emission to the total B band flux is taken into account in the calculation of the emission measure for the hot gas of the Local Bubble so that the B band flux still matches the all-sky average.

We note that no attempt is made to make this model consistent with the size of the local cavity, which is proposed to contain the hot gas in the standard model for the SXRb (e.g., Snowden et al. 1998). The pressure in the hot gas is not adjusted to fit such models. Rather the total pressure in the hot gas for an evaporating cloud model is dictated by the assumed density, temperature and magnetic field in the cloud. In fact the pressures in our models come out far too low for the standard model to produce the SXRb within the confines of the Local Cavity as deduced, e.g., from Na I observations (Lallement et al. 2003). This in turn means that if the thermal pressure in the Local Bubble turns out to be much lower than was assumed in those models because a substantial fraction of the SXRb comes from SWCX then the emission from the cloud boundary would be unaffected.

An example of the profiles of the hydrodynamic variables for two different models is shown in Fig. 2. The magnetic field strength in these calculations is assumed to be proportional to the density at every point in the outflow. The treatment here is the same as in Slavin (1989) which contains a more thorough discussion of the issues involved in this sort of calculation. The effect of the field on the conductivity is parametrized in a simple way by a constant reduction factor of 0.5. The importance of the magnetic field for our calculations lies in the way it affects the thermal pressure in the layer. Since the density drops sharply in the outflow and  $|B| \sim n$ , any magnetic pressure ( $\sim B^2$ ) drops even more sharply. The total pressure is roughly constant in the boundary, so the thermal pressure necessarily rises to make up for the decreasing magnetic pressure. Since all our models have nearly the same thermal pressure in the cloud, the primary effect of the magnetic field is to help determine the thermal pressure in the interface and thus radiative flux from the boundary. Since the total soft X-ray flux is fixed by requiring a match with the Wisconsin B band all-sky average count rate (McCammon et al. 1983), a larger assumed magnetic field increases only the EUV flux which is not constrained by the B-band data. The affect on the cloud of a larger EUV flux is to increase its temperature and ionization.

A secondary effect of the magnetic field can be seen in the temperature profiles in Figure 2. In evaporating clouds in the ISM, if the temperature gradient is large enough and the thermal pressure is low enough, the conduction becomes “saturated”, which means that the heat flux expected from the gas temperature and temperature gradient exceeds the flux that can be carried by the electrons (Cowie & McKee 1977). Saturation leads to a steepening of the temperature gradient and a relative slowing of the mass loss rate. In the two cases shown in Figure 2,

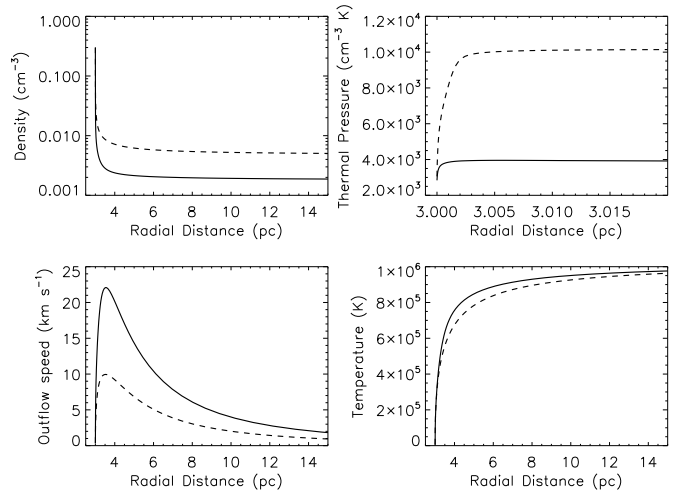


**Fig. 2.** Profiles of hydrodynamic variables in two different cloud boundary calculations. The solid lines are for model 6 which has  $n_{\text{H}} = 0.273 \text{ cm}^{-3}$ ,  $\log T_h = 6.0$ ,  $B_0 = 2 \mu\text{G}$  and  $N_{\text{HI}} = 4.5 \times 10^{17} \text{ cm}^{-2}$ , while the dashed lines are for model 8, which differs from model 6 only in the strength of the magnetic field,  $B_0 = 5 \mu\text{G}$ . Note that in the upper right panel, the plot of thermal pressure, the radial scale is much smaller in order to show the variation in thermal pressure. The higher magnetic pressure inside the cloud for model 8 leads to the higher external thermal pressure for that case. The temperature profile differs in the two cases because the degree of heat flux saturation is reduced for the higher thermal pressure of model 8, which in turn leads to a shallower temperature gradient.

the lower magnetic field case ( $B_0 = 2 \mu\text{G}$ ) is moderately saturated (in terms of Cowie & McKee’s parameter,  $\sigma_0 = 3$ ) while the other case ( $B_0 = 5 \mu\text{G}$ ), because of the higher magnetic pressure, is less saturated.

### 3. Photoionization Models

The photoionization models of the LIC are developed following the same underlying procedure as in SF02, but selecting only the LIC absorption component towards  $\epsilon \text{ CMa}$  for comparison. Improvements include using updated values for *in situ* ISM observations and using a recent version of the Cloudy radiative transfer/thermal equilibrium code (version 06.02.09a, Ferland et al. 1998). We run Cloudy with the assumption of a plane-parallel cloud geometry and format our calculated photoionizing spectrum to be used as input. The selected options include utilizing recent calculations for the dielectronic recombination rates for  $\text{Mg}^+ \rightarrow \text{Mg}^0$  (e.g. Altun et al. 2006, and the commands “set dielectronic recombination Badnell” and “set radiative recombination Badnell”), the assumption of constant pressure, and the inclusion of interstellar dust grains at 50% abundance compared to a standard ISM value. As we discuss below, the only role that dust plays is net heating of the gas since there is far too little column for extinction to be important (expected  $E(B - V) \sim 10^{-4.2}$ ). The fraction of the heating provided by dust is  $\sim 4\%$  of the total heating, while dust provides  $\sim 2\%$  of the cooling (mainly by capture of electrons onto grain surfaces). A cosmic ray ionization rate at the default background level of  $2.5 \times 10^{17} \text{ s}^{-1}$  (for H ionization) is included. The LIC is assumed to be in ionization and thermal equilibrium, and Cloudy calculates the detailed transfer of radiation, including absorption and

**Table 2.** Model Input Parameter Values

Model No.	Input Parameter			
	$n_{\text{H}}$ ( $\text{cm}^{-3}$ )	$\log T_h$ (K)	$B_0$ ( $\mu\text{G}$ )	$N_{\text{HI}}$ ( $10^{17} \text{cm}^{-2}$ )
1	0.273	5.9	2.0	3.0
2	0.273	5.9	2.0	4.5
3	0.273	5.9	5.0	3.0
4	0.273	5.9	5.0	4.5
5	0.273	6.0	2.0	3.0
6	0.273	6.0	2.0	4.5
7	0.273	6.0	5.0	3.0
8	0.273	6.0	5.0	4.5
9	0.273	6.1	2.0	3.0
10	0.273	6.1	2.0	4.5
11	0.273	6.1	5.0	3.0
12	0.273	6.1	5.0	4.5
13	0.218	5.9	2.0	3.0
14	0.218	5.9	2.0	4.5
15	0.218	5.9	5.0	3.0
16	0.218	5.9	5.0	4.5
17	0.218	6.0	2.0	3.0
18	0.218	6.0	2.0	4.5
19	0.218	6.0	5.0	3.0
20	0.218	6.0	5.0	4.5
21	0.218	6.1	2.0	3.0
22	0.218	6.1	2.0	4.5
23	0.218	6.1	5.0	3.0
24	0.218	6.1	5.0	4.5
25	0.226	5.9	4.7	3.0
26	0.213	5.9	2.5	4.0
27	0.226	6.0	3.8	3.0
28	0.216	6.0	2.1	4.0
29	0.232	6.1	3.4	3.0
30	0.223	6.1	0.05	4.0
42	0.218	6.1	–	4.5

scattering of the radiation incident on the cloud surface, as well as the diffuse continuum and emission lines generated within the cloud.

The procedure for creating a model begins with generating the incident radiation field at the cloud surface (§2.3). The radiative transfer model is then run, and the output predictions of the model are compared to observations of interstellar absorption lines in the LIC towards  $\epsilon$  CMa ( $N(\text{C II}^*)$ ,  $N(\text{N I})$ ,  $N(\text{O I})$ ,  $N(\text{Mg II})$ ,  $N(\text{S II})$ ,  $N(\text{Si II})$ ,  $N(\text{Fe II})$ ) and *in situ* observations of  $n(\text{He}^0)$  by spacecraft inside of the solar system. The abundances of C, N, O, Mg, Si, S and Fe are then adjusted to be consistent with the observed column densities. With these new abundances, the Cloudy run is repeated and this process is continued until no adjustment of the abundances is needed. Because the abundances do have an impact on the emission from the cloud boundary, the cloud evaporation model is then re-run with the new abundances as well to re-generate the input ionizing spectrum. The iterative process of generating the spectrum and doing the Cloudy photoionization runs generally requires only a couple runs of the cloud evaporation program and a few runs of Cloudy.

#### 4. Model Results

To investigate the dependence of the results on the input parameters we calculate a grid of 24 models. We explore total H density,  $n_{\text{H}} = 0.273, 0.218$ ; Local Bubble hot gas temperature,  $\log T_h = 5.9, 6.0, 6.1$ ; magnetic field strength,  $B_0 = 2, 5 \mu\text{G}$ ; and HI column density,  $N_{\text{HI}} = 3 \times 10^{17}, 4.5 \times 10^{17} \text{cm}^{-2}$ . The val-

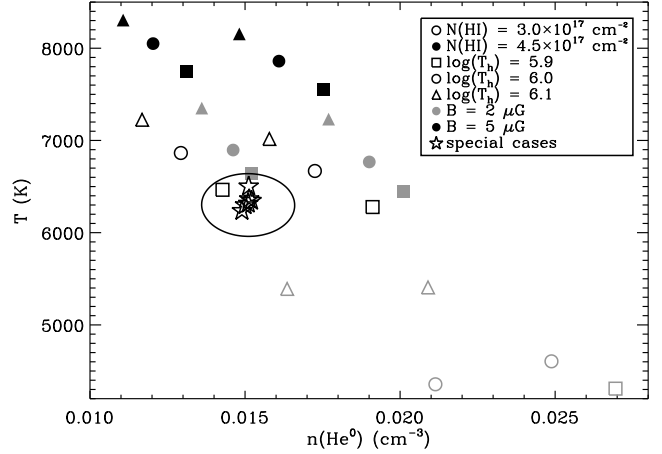


**Fig. 3.** Model results for the  $\text{He}^0$  density and temperature in the ISM just outside the heliosphere. The squares, circles, and triangles are for models that are part of the initial grid of 24 models, while the stars are for models 25 – 30 for which the magnetic field,  $B$ , and the total H density,  $n_{\text{H}}$ , were varied to match the observed  $n(\text{He}^0)$  and  $T$ . For the grid models, the empty symbols are for models with  $N(\text{HI}) = 3 \times 10^{17} \text{cm}^{-2}$ , while the filled symbol models have  $N(\text{HI}) = 4.5 \times 10^{17} \text{cm}^{-2}$ . As the legend shows, the color (black vs. gray) indicates the magnetic field strength and the symbol shape indicates the temperature assumed for the hot gas of the Local Bubble. For identical kinds of points, the one to the left is for a model with  $n(\text{H}^0) = 0.218 \text{cm}^{-3}$  and the one to the right has  $n(\text{H}^0) = 0.273 \text{cm}^{-3}$ . The ellipse is the error range around the observed values for  $n(\text{He}^0)$  and  $T$ .

ues for  $T$  and  $n(\text{He I})$  at the solar location, the endpoint of the calculations, are shown in Fig. 3 for this set of models. We then explore another six models in which we do the calculations over a grid in  $\log T_h$  and  $N_{\text{HI}}$  but vary the values of  $n_{\text{H}}$  and  $B_0$  in order to match the observed  $T$  and  $n(\text{He I})$ . We employed a multiple linear regression to assist in narrowing down the search region for the values of  $n_{\text{H}}$  and  $B_0$  needed to match the observations. Since the dependencies of the results on the parameters really are quite non-linear, this procedure could not work to predict exactly correct values for the required parameters, but was useful for getting close to the correct values. Based on the results for the initial grid of models, we use  $\log T_h = 5.9, 6.0, 6.1$  and  $N_{\text{HI}} = 3 \times 10^{17}, 4 \times 10^{17} \text{cm}^{-2}$  for this smaller grid, models 25 – 30. We chose to use  $4 \times 10^{17} \text{cm}^{-2}$  rather than  $4.5 \times 10^{17} \text{cm}^{-2}$  because the higher column density models, for the most part, produced temperatures that were too high. As can be seen from Fig. 3, all of these models (25–30), plotted as stars, are consistent with the observed  $T$  and  $n(\text{He I})$ , indicated by the ellipse in the figure. Table 2 gives the input parameters for each model. Model predictions for the  $\epsilon$  CMa sightline integrated through the LIC are presented in Table 3. Model predictions for the CHISM (i.e. at the solar location) are shown in Table 4.

In SF02 we tested models with no emission from the cloud boundary. This amounts to assuming that the boundary is a sharp transition from the hot gas of the Local Bubble to the warm gas of the LIC. We have again explored such models using the LIC data as constraints in the same way as for the models discussed above with a conductive interface. When there is no evaporative boundary, our models do not depend on the magnetic field in the cloud since in that case the ionizing flux consists only of diffuse emission from the hot gas of the Local Bubble and EUV

**Table 3.** Model Column Density Results

Model <sup>a</sup>	$\log N(\text{H}_{\text{tot}})$	$\log N(\text{Ar I})$	$\log N(\text{Ar II})$	$\log N(\text{Si III})$	$\frac{N(\text{Mg II})}{N(\text{Mg I})}$	$\frac{N(\text{C II})}{N(\text{C II}^*)}$	$\frac{N(\text{H I})}{N(\text{He I})}$
Obs. <sup>b</sup>	–	–	–	12.40	$443^{+197}_{-110}$	93 – 430 <sup>c</sup>	12 – 16
1	17.58	11.48	11.76	8.895	706.3	213.0	11.36
2	17.78	11.67	11.95	9.641	325.3	234.1	11.40
3	17.65	11.33	11.84	9.844	246.1	182.1	11.44
4	17.82	11.55	12.00	10.12	136.5	198.0	11.80
5	17.58	11.49	11.75	8.961	717.8	230.0	11.62
6	17.78	11.67	11.94	9.711	286.7	244.9	11.62
7	17.64	11.34	11.81	9.909	207.4	194.8	12.47
8	17.82	11.56	11.97	10.17	119.7	208.2	12.66
9	17.59	11.46	11.75	9.289	553.0	239.5	12.27
10	17.78	11.66	11.93	9.861	210.3	248.1	12.14
11	17.64	11.33	11.78	9.993	171.2	201.7	13.44
12	17.82	11.54	11.95	10.23	104.3	210.6	13.52
13	17.60	11.44	11.78	9.100	768.9	255.1	11.52
<b>14</b>	17.79	11.64	11.96	9.738	336.4	274.4	11.47
15	17.67	11.30	11.85	9.944	251.2	215.9	11.65
16	17.84	11.51	12.01	10.21	140.6	232.1	12.01
17	17.58	11.47	11.76	8.926	840.1	262.5	11.65
18	17.79	11.65	11.95	9.792	308.9	286.3	11.64
19	17.66	11.30	11.82	10.02	208.5	229.2	12.76
20	17.84	11.52	11.98	10.26	123.5	242.1	12.95
21	17.59	11.43	11.76	9.318	633.1	280.8	12.41
22	17.79	11.63	11.94	9.926	224.9	288.4	12.25
23	17.66	11.29	11.79	10.10	175.0	235.5	13.81
24	17.84	11.50	11.96	10.31	110.2	245.5	13.85
25	17.66	11.32	11.84	9.887	271.3	213.6	11.71
<b>26</b>	17.74	11.56	11.91	9.676	383.9	270.1	11.70
<b>27</b>	17.63	11.36	11.79	9.751	331.1	242.0	12.51
<b>28</b>	17.73	11.59	11.90	9.625	411.6	284.5	11.79
<b>29</b>	17.62	11.38	11.77	9.720	329.3	251.6	13.01
<b>30</b>	17.72	11.60	11.88	9.642	386.6	295.1	12.08
<b>42</b>	17.77	11.70	11.92	9.555	482.9	317.9	11.51

<sup>a</sup> The best models, consistent with all observational data (see §4), are indicated by bold face.

<sup>b</sup> Observational results from Gry & Jenkins (2001) (see table 1). The values listed for  $N(\text{H I})/N(\text{He I})$  are the range of values observed excluding Feige 24 which is one of the most distant stars observed by Dupuis et al. (1995) and has unusually large  $N(\text{H I})$  and ratio values.

<sup>c</sup> The upper limit on  $N(\text{C II})$  is not well determined observationally because of the saturation of the line. Gry & Jenkins (2001) define it by assuming a solar C/S abundance ratio and using the observed S II column density. We find (see Slavin & Frisch 2006) that the abundance of C required to match the  $N(\text{C II}^*)$  observations is supersolar, with C/S  $\sim 36 - 44$ , which results in a much higher upper limit on  $N(\text{C II})$ .

emission from nearby hot stars and the spectrum is not related to the properties of the cloud. For these models our model grid consists of total H density,  $n_{\text{H}} = 0.273, 0.218$ , Local Bubble hot gas temperature,  $\log T_h = 5.9, 6.0, 6.1$ , and H I column density,  $N_{\text{HI}} = 3 \times 10^{17}, 4.5 \times 10^{17} \text{ cm}^{-2}$ , for a total of twelve models that we label as models 31–42. Of these models, however, only two resulted in ionizing fluxes sufficient to heat the cloud to a temperature  $\sim 6000$  K at the same time as matching the constraints on the ion column densities. These models were the ones with  $\log T_h = 6.1$  and  $N_{\text{HI}} = 4.5 \times 10^{17} \text{ cm}^{-2}$  (models 36 and 42). For the other cases, either at the surface or deeper into the cloud, there are insufficient photons to provide the heating to balance the cooling and the cloud temperature drops sharply to  $< 1000$  K. The model with  $n_{\text{H}} = 0.218$  (model 42) is consistent with the observed value of  $n(\text{He}^0)$  and with the column density data as well.

From these 42 models we have selected those that provide acceptable results for the observational constraints, according to prioritized requirements. The first requirement is that the model predict the density and temperature of He I observed inside of the solar system. Models 14 (marginally), 15 and 25–30 and 42 predict a He density and temperature consistent with the ob-

served values within the reported errors. They also predict the PUI Ne densities, for an assumed Ne/H=123 ppm. Models 26 and 28 successfully match the PUI data for Ne/H as low as  $\sim 100$  ppm. These models are also required to match the observed Mg II/Mg I ratio in the LIC towards  $\epsilon$  CMa. Models 14, 27, and 29 marginally fit this criterion, while 26, 28, 30, and 42 successfully fit this criterion. Note that the new models now provide acceptable predictions for the CHISM temperature, which was not the case for the best models in SF02. These models are also consistent with the observed C II/C II\* ratios in the LIC component towards  $\epsilon$  CMa though this constraint is weak because of the large uncertainties in  $N(\text{C II})$ . Based on these comparisons, and given the uncertainties in both data and models, Models 14, 26–30, and 42 are plausible models, but Models 26 and 28 appear to best match the observational constraints.

Based on the constraints and assumptions presented in the previous section, we select models 14, 26–30 and 42 as the best models for the LIC ionization, with models 26 and 28 favored by the PUI Ne data provided that Ne/H  $> 100$  ppm. We believe that these seven models then give a realistic range for the uncertainties in the boundary conditions of the heliosphere, providing that the underlying assumptions implicit in the Cloudy code, e.g.

**Table 4.** Model Results for Solar Location

Model <sup>a</sup>	X(H)	X(He)	$n(\text{H}^0)$	$n(\text{He}^0)$	$n(\text{N}^0)$	$n(\text{O}^0)$	$n(\text{Ne}^0)$	$n(\text{Ar}^0)$	$n_e$	$n_p$	$T$
Obs. <sup>b</sup>				0.015	$5.5 \times 10^{-6}$	$4.8 \times 10^{-5}$	$5.8 \times 10^{-6}$	$1.6 \times 10^{-7}$			6300
1	0.176	0.299	0.318	0.0269	$1.84 \times 10^{-5}$	$1.48 \times 10^{-4}$	$1.39 \times 10^{-5}$	$3.47 \times 10^{-7}$	0.0800	0.0678	4310
2	0.196	0.352	0.251	0.0201	$9.63 \times 10^{-6}$	$7.71 \times 10^{-5}$	$8.51 \times 10^{-6}$	$2.69 \times 10^{-7}$	0.0724	0.0611	6450
3	0.286	0.404	0.230	0.0191	$1.34 \times 10^{-5}$	$1.07 \times 10^{-4}$	$7.81 \times 10^{-6}$	$1.82 \times 10^{-7}$	0.106	0.0922	6280
4	0.259	0.428	0.229	0.0175	$8.86 \times 10^{-6}$	$6.95 \times 10^{-5}$	$6.45 \times 10^{-6}$	$1.92 \times 10^{-7}$	0.0937	0.0799	7560
5	0.174	0.310	0.300	0.0249	$1.72 \times 10^{-5}$	$1.39 \times 10^{-4}$	$1.13 \times 10^{-5}$	$3.30 \times 10^{-7}$	0.0750	0.0631	4610
6	0.197	0.363	0.242	0.0190	$9.13 \times 10^{-6}$	$7.44 \times 10^{-5}$	$7.08 \times 10^{-6}$	$2.61 \times 10^{-7}$	0.0707	0.0593	6770
7	0.278	0.441	0.225	0.0173	$1.33 \times 10^{-5}$	$1.04 \times 10^{-4}$	$5.75 \times 10^{-6}$	$1.78 \times 10^{-7}$	0.101	0.0866	6670
8	0.257	0.459	0.223	0.0161	$8.65 \times 10^{-6}$	$6.79 \times 10^{-5}$	$4.92 \times 10^{-6}$	$1.89 \times 10^{-7}$	0.0918	0.0773	7860
9	0.193	0.357	0.265	0.0209	$1.53 \times 10^{-5}$	$1.23 \times 10^{-4}$	$7.52 \times 10^{-6}$	$2.71 \times 10^{-7}$	0.0761	0.0634	5410
10	0.203	0.392	0.235	0.0177	$9.06 \times 10^{-6}$	$7.24 \times 10^{-5}$	$5.52 \times 10^{-6}$	$2.43 \times 10^{-7}$	0.0723	0.0600	7230
11	0.278	0.474	0.220	0.0158	$1.29 \times 10^{-5}$	$1.02 \times 10^{-4}$	$4.42 \times 10^{-6}$	$1.69 \times 10^{-7}$	0.0999	0.0847	7020
12	0.262	0.490	0.219	0.0148	$8.41 \times 10^{-6}$	$6.66 \times 10^{-5}$	$3.83 \times 10^{-6}$	$1.78 \times 10^{-7}$	0.0928	0.0776	8160
13	0.201	0.333	0.230	0.0191	$1.34 \times 10^{-5}$	$1.08 \times 10^{-4}$	$8.94 \times 10^{-6}$	$2.32 \times 10^{-7}$	0.0681	0.0580	4720
<b>14</b>	0.215	0.376	0.193	0.0152	$7.29 \times 10^{-6}$	$5.95 \times 10^{-5}$	$5.99 \times 10^{-6}$	$1.94 \times 10^{-7}$	0.0625	0.0528	6650
15	0.310	0.436	0.176	0.0143	$1.02 \times 10^{-5}$	$8.18 \times 10^{-5}$	$5.35 \times 10^{-6}$	$1.28 \times 10^{-7}$	0.0905	0.0789	6470
16	0.284	0.461	0.175	0.0131	$6.76 \times 10^{-6}$	$5.36 \times 10^{-5}$	$4.40 \times 10^{-6}$	$1.35 \times 10^{-7}$	0.0812	0.0695	7750
17	0.178	0.315	0.255	0.0211	$1.47 \times 10^{-5}$	$1.19 \times 10^{-4}$	$9.51 \times 10^{-6}$	$2.75 \times 10^{-7}$	0.0656	0.0553	4360
18	0.214	0.383	0.188	0.0146	$7.16 \times 10^{-6}$	$5.81 \times 10^{-5}$	$5.07 \times 10^{-6}$	$1.91 \times 10^{-7}$	0.0610	0.0513	6900
19	0.302	0.472	0.173	0.0129	$1.01 \times 10^{-5}$	$8.03 \times 10^{-5}$	$3.93 \times 10^{-6}$	$1.26 \times 10^{-7}$	0.0872	0.0748	6860
20	0.282	0.491	0.172	0.0120	$6.61 \times 10^{-6}$	$5.26 \times 10^{-5}$	$3.37 \times 10^{-6}$	$1.33 \times 10^{-7}$	0.0802	0.0677	8050
21	0.204	0.374	0.211	0.0164	$1.20 \times 10^{-5}$	$9.85 \times 10^{-5}$	$5.54 \times 10^{-6}$	$2.04 \times 10^{-7}$	0.0648	0.0541	5390
22	0.221	0.414	0.184	0.0136	$6.96 \times 10^{-6}$	$5.69 \times 10^{-5}$	$3.90 \times 10^{-6}$	$1.78 \times 10^{-7}$	0.0628	0.0523	7350
23	0.305	0.506	0.168	0.0117	$9.91 \times 10^{-6}$	$7.82 \times 10^{-5}$	$2.97 \times 10^{-6}$	$1.18 \times 10^{-7}$	0.0868	0.0737	7220
24	0.286	0.520	0.169	0.0111	$6.57 \times 10^{-6}$	$5.16 \times 10^{-5}$	$2.60 \times 10^{-6}$	$1.25 \times 10^{-7}$	0.0808	0.0676	8310
25	0.297	0.427	0.187	0.0151	$1.09 \times 10^{-5}$	$8.67 \times 10^{-5}$	$5.75 \times 10^{-6}$	$1.41 \times 10^{-7}$	0.0907	0.0789	6360
<b>26</b>	0.224	0.385	0.192	0.0151	$8.32 \times 10^{-6}$	$6.66 \times 10^{-5}$	$5.96 \times 10^{-6}$	$1.83 \times 10^{-7}$	0.0653	0.0554	6320
<b>27</b>	0.258	0.426	0.195	0.0149	$1.13 \times 10^{-5}$	$8.97 \times 10^{-5}$	$5.03 \times 10^{-6}$	$1.63 \times 10^{-7}$	0.0796	0.0677	6240
<b>28</b>	0.212	0.376	0.194	0.0152	$8.24 \times 10^{-6}$	$6.73 \times 10^{-5}$	$5.49 \times 10^{-6}$	$1.95 \times 10^{-7}$	0.0622	0.0523	6350
<b>29</b>	0.242	0.429	0.202	0.0150	$1.17 \times 10^{-5}$	$9.30 \times 10^{-5}$	$4.53 \times 10^{-6}$	$1.74 \times 10^{-7}$	0.0769	0.0646	6300
<b>30</b>	0.203	0.379	0.197	0.0151	$8.51 \times 10^{-6}$	$6.81 \times 10^{-5}$	$4.78 \times 10^{-6}$	$2.01 \times 10^{-7}$	0.0605	0.0502	6500
<b>42</b>	0.189	0.355	0.186	0.0145	$6.91 \times 10^{-6}$	$5.71 \times 10^{-5}$	$4.60 \times 10^{-6}$	$2.04 \times 10^{-7}$	0.0522	0.0433	6590

<sup>a</sup> The best models (see §4) are indicated by bold face.

<sup>b</sup> Observational results from Gloeckler & Geiss (2004), Gloeckler (2005, private communication) and Witte et al. (1996) (see table 1 for uncertainties).

photoionization equilibrium, are correct. The predictions of the best models provide excellent matches to the observational constraints. Based on these models, we find the boundary conditions of the heliosphere to be describable as  $n(\text{H}^0) = 0.19 - 0.20 \text{ cm}^{-3}$ ,  $n_e = 0.05 - 0.08 \text{ cm}^{-3}$ , and  $X(\text{H}) \equiv \text{H}^+ / (\text{H}^0 + \text{H}^+) = 0.19 - 0.26$ ,  $X(\text{He}) \equiv \text{He}^+ / (\text{He}^0 + \text{He}^+) = 0.36 - 0.43$ . For these models, we find abundances of  $\text{O}/\text{H} = 295 - 437 \text{ ppm}$ ,  $\text{C}/\text{H} = 589 - 813 \text{ ppm}$ , and  $\text{N}/\text{H} = 40.7 - 64.6 \text{ ppm}$  (Table 7). The total LIC density is  $n(\text{H})_0 = 0.213 - 0.232 \text{ cm}^{-3}$ , while the strength of the interstellar magnetic in the cloud varies between 0 and  $3.8 \mu\text{G}$ . The Ne PUI data further favor densities of  $n(\text{H}^0) \approx 0.19 \text{ cm}^{-3}$  and  $n_e = 0.06 - 0.07 \text{ cm}^{-3}$ .

In this analysis we have assumed negligible filtration for He in the heliosheath regions. Modeling of the He filtration factor however allows values as small as  $f_{\text{He}} = 0.92$ , which yields  $n(\text{He I}) = 0.0164 \text{ cm}^{-3}$  for the CHISM (Table 1). The predictions of Model 21 agree with this value for  $n(\text{He I})$ , as well as with the ratios  $\text{Mg II}/\text{Mg I}$  and  $\text{C II}/\text{C I}^*$  towards  $\epsilon \text{ CMa}$  and the pickup ion Ne and Ar data (Table 3). The predicted cloud temperature is low by  $\sim 1000 \text{ K}$ . The density and ionization for Model 21 are  $n(\text{H}^0) = 0.21 \text{ cm}^{-3}$  and  $n_e = 0.06 \text{ cm}^{-3}$ . We therefore conclude that our best models listed above are robust in the sense that they predict consistent values for the  $n(\text{H}^0)$  to within 5%, and electron densities to within 25%.

The radiation field incident on the LIC for Model 26 is shown in Fig. 1 and the spectral characteristics of the field for each model are listed in Table 5. The wavelengths regions  $\lambda \leq 912 \text{ \AA}$  and  $\lambda \sim 1500 \text{ \AA}$  are of primary importance for the photoionization of the cloud, the former because it determines  $\text{H}^0$  and  $\text{He}^0$  ionization, and the latter because it determines  $\text{Mg}^0$  ionization.

The ionization parameter is defined as  $U \equiv \Phi / n(\text{H})c$ , where  $\Phi$  is the H ionizing photon flux,  $n(\text{H})$  is the total (neutral + ionized) hydrogen density at the cloud surface and  $c$  is the speed of light. The total ionizing photon fluxes at the cloud surface (photons  $\text{cm}^{-2} \text{ s}^{-1}$ ) for the three bands 13.6–24.6, 24.6–54.4, and 54.4–100 eV, are given by  $\Phi_{\text{H}}$ ,  $\Phi_{\text{He}^0}$ , and  $\Phi_{\text{He}^+}$ , respectively. The ratio of the total number of  $\text{H}^0$  and  $\text{He}^0$  ionizing photons in the incident radiation field is given by  $Q(\text{He}^0)/Q(\text{H}^0)$ . The quantity  $\langle E \rangle$  (eV) is the mean energy of an ionizing photon, equal to the integrated energy flux from 13.6 to 100 eV divided by the integrated photon flux over the same energy range.

In Figure 3 we show  $n(\text{He}^0)$  and temperature of the CHISM for our model calculations. In Figure 4 we show  $\text{N II}/\text{N I}$  vs.  $\text{Mg II}/\text{Mg I}$ , illustrating an anti-correlation of the ratios caused by the fact that  $\text{Mg II}/\text{Mg I}$  decreases with electron density while  $\text{N II}/\text{N I}$  indicates the ionization level in the cloud. The ionization of the CHISM is listed in Table 6 for Model 26, where commonly observed elements are listed. The abundances of He, Ne,

**Table 5.** Characteristics of the Model Radiation Field

Model <sup>a</sup>	U	$\phi_{\text{H}}$ photons $\text{cm}^{-2} \text{s}^{-1}$	$\phi_{\text{He}^0}$ photons $\text{cm}^{-2} \text{s}^{-1}$	$\phi_{\text{He}^+}$ photons $\text{cm}^{-2} \text{s}^{-1}$	$Q(\text{He}^0)/Q(\text{H}^0)$	$\langle E \rangle$ eV
1	$2.0 \times 10^{-6}$	$4.6 \times 10^3$	$7.5 \times 10^3$	$2.8 \times 10^3$	0.46	74.6
2	$2.0 \times 10^{-6}$	$5.3 \times 10^3$	$7.3 \times 10^3$	$2.7 \times 10^3$	0.44	72.4
3	$3.1 \times 10^{-6}$	$9.0 \times 10^3$	$1.3 \times 10^4$	$2.7 \times 10^3$	0.49	57.7
4	$3.0 \times 10^{-6}$	$8.6 \times 10^3$	$1.2 \times 10^4$	$2.6 \times 10^3$	0.49	58.6
5	$2.0 \times 10^{-6}$	$4.0 \times 10^3$	$7.0 \times 10^3$	$3.8 \times 10^3$	0.43	79.0
6	$2.1 \times 10^{-6}$	$4.9 \times 10^3$	$6.9 \times 10^3$	$3.8 \times 10^3$	0.41	76.2
7	$3.2 \times 10^{-6}$	$7.4 \times 10^3$	$1.4 \times 10^4$	$3.8 \times 10^3$	0.53	61.3
8	$3.1 \times 10^{-6}$	$7.4 \times 10^3$	$1.3 \times 10^4$	$3.7 \times 10^3$	0.52	61.5
9	$2.2 \times 10^{-6}$	$3.8 \times 10^3$	$7.4 \times 10^3$	$5.6 \times 10^3$	0.40	80.0
10	$2.3 \times 10^{-6}$	$4.8 \times 10^3$	$7.2 \times 10^3$	$5.6 \times 10^3$	0.38	77.3
11	$3.5 \times 10^{-6}$	$6.6 \times 10^3$	$1.5 \times 10^4$	$5.6 \times 10^3$	0.53	63.4
12	$3.4 \times 10^{-6}$	$6.9 \times 10^3$	$1.5 \times 10^4$	$5.5 \times 10^3$	0.52	63.2
13	$2.3 \times 10^{-6}$	$4.3 \times 10^3$	$7.0 \times 10^3$	$2.8 \times 10^3$	0.46	76.9
<b>14</b>	$2.4 \times 10^{-6}$	$5.1 \times 10^3$	$6.8 \times 10^3$	$2.7 \times 10^3$	0.43	74.3
15	$3.7 \times 10^{-6}$	$8.5 \times 10^3$	$1.2 \times 10^4$	$2.7 \times 10^3$	0.49	58.8
16	$3.6 \times 10^{-6}$	$8.2 \times 10^3$	$1.2 \times 10^4$	$2.6 \times 10^3$	0.49	59.5
17	$2.3 \times 10^{-6}$	$3.7 \times 10^3$	$6.4 \times 10^3$	$3.8 \times 10^3$	0.42	81.8
18	$2.4 \times 10^{-6}$	$4.7 \times 10^3$	$6.2 \times 10^3$	$3.8 \times 10^3$	0.39	78.4
19	$3.9 \times 10^{-6}$	$7.1 \times 10^3$	$1.4 \times 10^4$	$3.8 \times 10^3$	0.53	62.2
20	$3.8 \times 10^{-6}$	$7.2 \times 10^3$	$1.3 \times 10^4$	$3.7 \times 10^3$	0.52	62.2
21	$2.6 \times 10^{-6}$	$3.6 \times 10^3$	$6.8 \times 10^3$	$5.6 \times 10^3$	0.39	82.0
22	$2.7 \times 10^{-6}$	$4.6 \times 10^3$	$6.6 \times 10^3$	$5.6 \times 10^3$	0.36	78.9
23	$4.2 \times 10^{-6}$	$6.3 \times 10^3$	$1.5 \times 10^4$	$5.6 \times 10^3$	0.52	64.4
24	$4.2 \times 10^{-6}$	$6.7 \times 10^3$	$1.4 \times 10^4$	$5.5 \times 10^3$	0.51	64.1
25	$3.5 \times 10^{-6}$	$7.9 \times 10^3$	$1.2 \times 10^4$	$2.7 \times 10^3$	0.49	60.3
<b>26</b>	$2.5 \times 10^{-6}$	$5.0 \times 10^3$	$7.5 \times 10^3$	$2.7 \times 10^3$	0.45	73.2
<b>27</b>	$3.1 \times 10^{-6}$	$5.4 \times 10^3$	$1.0 \times 10^4$	$3.8 \times 10^3$	0.50	68.9
<b>28</b>	$2.4 \times 10^{-6}$	$4.3 \times 10^3$	$6.4 \times 10^3$	$3.8 \times 10^3$	0.40	79.5
<b>29</b>	$3.0 \times 10^{-6}$	$4.6 \times 10^3$	$9.7 \times 10^3$	$5.6 \times 10^3$	0.45	73.6
<b>30</b>	$2.4 \times 10^{-6}$	$3.8 \times 10^3$	$5.5 \times 10^3$	$5.6 \times 10^3$	0.33	84.6
<b>42</b>	$2.2 \times 10^{-6}$	$3.6 \times 10^3$	$3.6 \times 10^3$	$5.6 \times 10^3$	0.25	91.1

<sup>a</sup> The best models (see §4) are indicated by bold face.

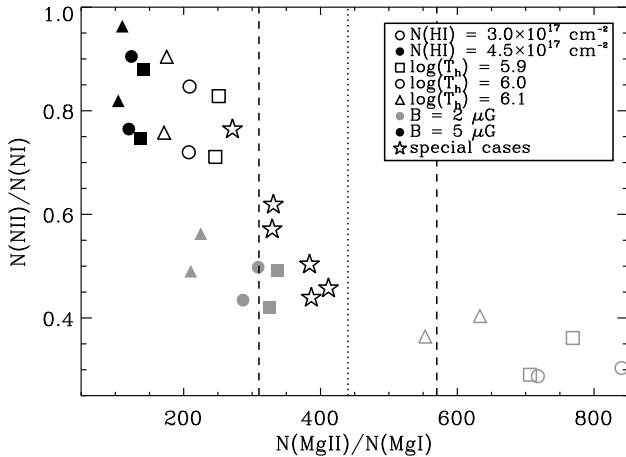


**Fig. 4.** Model results for  $N(\text{NII})/N(\text{NI})$  versus  $\text{Mg II}/\text{Mg I}$ . The symbols have the same meaning as in Figure 3. In this case the models with higher  $n(\text{H}^0)$  lie below and slightly to the left of those with lower density.  $N(\text{NII})/N(\text{NI})$  is an indicator of cloud ionization fraction while  $\text{Mg II}/\text{Mg I}$  goes as  $1/n_e$ . The dotted line is the observed value for  $\text{Mg II}/\text{Mg I}$  and the dashed lines indicate the  $1 - \sigma$  error range for the value. We see that models that match the observed ratio all correspond to relatively low ionization,  $X(\text{H}) \sim 0.20 - 0.27$  in the CHISM.

Na, Al, P, Ar, and Ca were assumed, based on solar abundances, and were not adjusted in the modeling process. The abundances of C, N, O, Mg, Si, S and Fe were adjusted for each model to match observed column densities towards  $\epsilon$  Cma (see §2). The elemental abundances that have been assumed, with the exception of that for He, are not expected to have any significant impact on the model results.

## 5. Discussion

### 5.1. Heliosphere Boundary Conditions

As discussed above, the best models of those we calculated are determined by the match to the CHISM  $\text{He}^0$  density and temperature found by the *in situ* Ulysses measurements (§2.2), combined with the matching the LIC component column density ratios  $\text{Mg II}/\text{Mg I}$  and  $\text{C II}/\text{C II}^*$ . These models span a fairly large range in the model parameters:  $n_{\text{H}} = 0.213 - 0.232 \text{ cm}^{-3}$ ,  $\log T_h = 5.9 - 6.1 \text{ K}$ ,  $B_0 = 0.05 - 3.8 \mu\text{G}$ , and  $N(\text{H I}) = 3.0 \times 10^{17} - 4.5 \times 10^{17} \text{ cm}^{-2}$ . Despite this, the predicted values for neutral H density and electron density in the CHISM lie within a remarkably small range:  $n(\text{H}^0) = 0.19 - 0.20 \text{ cm}^{-3}$ ,  $n_e = 0.05 - 0.08 \text{ cm}^{-3}$ , for models that include the conductive boundary. For the one model without evaporation that is consistent with the data we find  $n(\text{H}^0) = 0.186 \text{ cm}^{-3}$ ,  $n_e = 0.052 \text{ cm}^{-3}$ . Including the PUI Ne data as a constraint narrows the density results to  $n(\text{H}^0) \approx 0.19 \text{ cm}^{-3}$  and  $n_e = 0.06 - 0.07 \text{ cm}^{-3}$ . For these

**Table 6.** Model 26 Results for Ionization Fractions<sup>a</sup>

Element	PPM	I	II	III	IV
H	10 <sup>6</sup>	0.776	0.224	–	–
He	10 <sup>5</sup>	0.611	0.385	4.36(-3)	–
C	661	2.68(-4)	0.975	0.0244	0.000
N	46.8	0.720	0.280	8.52(-5)	0.000
O	331	0.814	0.186	4.71(-5)	0.000
Ne	123	0.196	0.652	0.152	2.79(-6)
Na	2.04	1.47(-3)	0.843	0.155	6.34(-6)
Mg	6.61	1.98(-3)	0.850	0.148	0.000
Al	0.0794	5.37(-5)	0.976	0.0118	0.0123
Si	8.13	4.21(-5)	0.999	8.02(-4)	3.10(-5)
P	0.219	1.35(-4)	0.977	0.0232	9.29(-5)
S	15.8	6.47(-5)	0.971	0.0288	1.95(-6)
Ar	2.82	0.263	0.500	0.238	2.83(-6)
Ca	4.07(-4)	9.21(-6)	0.0155	0.984	1.87(-4)
Fe	2.51	7.01(-5)	0.975	0.0245	5.75(-6)

<sup>a</sup> Numbers less than 10<sup>-3</sup> are written as x(y) where y is the exponent and x is the mantissa (or significant).

densities to stray out of this range would appear to require significant errors in the underlying comparison data, e.g.  $n(\text{He}^0)$  in the CHISM, or substantial non-equilibrium ionization effects in the LIC. The variation in the interstellar radiation field between the different models that match the data give us some degree of confidence that these densities are not highly sensitive to the details of the radiation field. The range  $n_e = 0.05 - 0.08 \text{ cm}^{-3}$  corresponds to an electron plasma frequency of 2.0–2.5 kHz, which is the frequency of the mysterious weak radio emission detected beyond the termination shock in the outer heliosphere (Gurnett & Kurth 2005; Mitchell et al. 2004).

## 5.2. Hydrogen Filtration Factor

Tracers of  $\text{H}^0$  inside of the termination shock, after filtration, include the  $\text{H I Ly}\alpha$  backscattered radiation, H pickup ions, and the slowdown of the solar wind at distances beyond 5 AU from mass-loading by H PUIs. The range of  $n(\text{H}^0)$  found above to best fit the combined heliospheric  $n(\text{He}^0)$  and LIC data towards  $\epsilon \text{ CMa}$ ,  $n(\text{H}^0) = 0.19 - 0.20 \text{ cm}^{-3}$ , represents the density of neutral interstellar H atoms outside of the heliosphere, and removed from heliospheric influences. The hydrogen filtration factor,  $f_H$ , can be obtained from comparisons between these models and interstellar  $\text{H}^0$  densities at the termination shock as inferred from in situ observations of interstellar H inside of the heliosphere.

The accompanying papers in this special section provide estimates of the interstellar  $\text{H}^0$  density at the termination shock. The solar wind slows down due to massloading by interstellar H, yielding  $n(\text{H}^0) = 0.09 \pm 0.01 \text{ cm}^{-3}$  at the termination shock (Richardson et al. 2007). The density of H pickup ions observed by Ulysses is inferred at the termination shock, yielding  $n(\text{H}^0) = 0.11 \pm 0.01 \text{ cm}^{-3}$ ; models of H atoms traversing the heliosheath regions then yield for the CHISM  $n(\text{H}^0) = 0.20 \pm 0.02 \text{ cm}^{-3}$  and  $n_p = 0.04 \pm 0.02 \text{ cm}^{-3}$ , or  $n_e \sim 0.05 \text{ cm}^{-3}$  (Bzowski et al. 2007). The radial variation in the response of the interplanetary  $\text{Ly}\alpha$  1215 Å backscattered radiation to the solar rotational modulation of the  $\text{Ly}\alpha$  “beam” that excites the fluorescence yields  $n(\text{H}^0) \sim 0.085 - 0.095 \text{ cm}^{-3}$ , depending on the heliosphere model (Pryor et al. 2007). From these  $n(\text{H}^0)$  values at the termination shock, we estimate that 43%–58% of the H-atoms successfully traverse the heliosheath region, or  $f_H \sim 0.43 - 0.58$ . Müller et al. (2007) evaluate filtration using five different plasma-neutral

**Table 7.** Elemental Gas Phase Abundances (ppm)

Model No.	Element						
	C	N	O	Mg	Si	S	Fe
14	589	40.7	295	5.89	7.24	14.1	2.24
21	955	60.3	447	9.77	11.5	22.9	3.55
25	631	66.1	437	7.76	10.0	19.5	3.09
26	661	46.8	331	6.61	8.13	15.8	2.51
27	759	64.6	437	8.71	10.7	20.9	3.31
28	708	45.7	331	7.08	8.32	16.6	2.57
29	813	64.6	437	9.33	11.0	21.9	3.39
30	741	46.8	331	7.41	8.51	17.0	2.63
42	724	39.8	295	6.76	7.76	15.1	2.34

models, and find a range of  $f_H = 0.52 - 0.74$ . A hydrogen filtration of  $f_H = 0.55 \pm 0.03$  is consistent with both in situ data and radiative transfer models.

## 5.3. Gas-Phase Abundances

The LIC photoionization models are forced to match the observed set of column densities (Tables 1 and 3). The gas-phase abundances of most elements are treated as free parameters that can be varied in order to match observed column densities, so that the successful models yield elemental abundances for the LIC that are automatically corrected for unobserved  $\text{H}^+$  (Table 7). The exceptions are that He, Ne, and Ar abundances, being unconstrained by the observations toward  $\epsilon \text{ CMa}$ , are not adjusted but are assumed to be 10<sup>5</sup> ppm, 123 ppm and 2.82 ppm, respectively. In the models,  $N(\text{C II}^*)$  is a constraint on both the C abundance (in place of the heavily saturated C II 1335 Å line) and  $n_e$ , such that the product of the abundance and  $n_e$  is more tightly limited than either quantity individually. The requirement to match both  $N(\text{C II}^*)$  and  $n(\text{He}^0)$  effectively restricts the ionization fraction of H, which in turn limits O and N ionization whose ionization fractions are tied by charge-transfer to the H ionization at LIC temperatures.

Early studies showed that the abundances of refractory elements in the very local ISM are enhanced compared to abundances in cold disk gas (Marschall & Hobbs 1972; Stokes 1978; Frisch 1981). Throughout warm and cold disk gas, the underabundances of refractory elements compared to solar abundances (by factors of 10<sup>-1</sup> – 10<sup>-4</sup>) are taken to represent depletion onto interstellar dust grains (e.g. Savage & Sembach 1996). This view is supported by the correlation found between elemental depletions and the temperature characteristic of condensation at solar pressure and composition (Ebel 2000), and assumes that there is a reference abundance pattern that characterizes the cloud, and remains constant over the cloud lifetime as atoms are exchanged between the gas and dust phases. Below (§5.4) we compare solar abundances with observed gas-phase abundances to predict the gas-to-dust mass ratios for the LIC, based on the assumption that LIC gas and dust have remained coupled over the cloud lifetime.

An important question is whether the LIC has solar abundances. Isotopes of <sup>18</sup>O and <sup>22</sup>Ne isotopes measured in the ACR population suggest that this is so. ACRs are characterized by a rising particle flux for energies below 10–50 MeV/nucleon, and this characteristic spectral signature is seen for <sup>16</sup>O, <sup>18</sup>O, <sup>20</sup>Ne, and <sup>22</sup>Ne. Ratios of <sup>16</sup>O/<sup>18</sup>O  $\sim$  500 and <sup>20</sup>Ne/<sup>22</sup>Ne  $\sim$  13.7 are found for both the ACRs and solar material, indicating that the CHISM and solar material have similar composi-

**Table 8.** Solar Abundances (ppm)

	Grevesse Sauval (1998)	Holweger (2001)	Lodders (2003)	Grevesse et al. (2007) <sup>a</sup>
C	334 ± 46	391(+110, -86)	290 ± 27	275 ± 34
N	84 ± 12	85.3 <sup>+25</sup> <sub>-19</sub>	82 ± 20	67 ± 10
O	683 ± 94	545 <sup>+107</sup> <sub>-90</sub>	579 ± 66	513 ± 63
Ne	121 ± 17	100 <sup>+17</sup> <sub>-15</sub>	91 ± 21	77 ± 12
Mg	38 ± 4	34.5 <sup>+5.1</sup> <sub>-4.5</sub>	41 ± 2	38 ± 9
Si	35 ± 4	34.4 <sup>+4.1</sup> <sub>-3.7</sub>	41 ± 2	36 ± 4
S	22 ± 5	-	18 ± 2	15 ± 2
Ar	2.54 ± 0.35	-	4.24 ± 0.77	1.70 ± 0.34
Fe	32 ± 4	28.1 <sup>+5.8</sup> <sub>-4.8</sub>	35 ± 2	32 ± 4

<sup>a</sup> Protosolar abundances are obtained by increasing the photospheric abundances by 0.05 dex for elements heavier than He, as suggested by Grevesse et al. (2007)

tions (Leske et al. 2000; Leske 2000). We therefore adopt solar abundances as the underlying reference abundance pattern for the LIC.

Unfortunately a prominent uncertainty exists in the correct solar abundances of volatile elements such as O and S, which have low condensation temperatures ( $T_{\text{cond}}$ , 180 K and 700 K respectively), and noble elements such as Ne and Ar. Solar abundances are determined from photospheric data (C, N, O, Mg, Si, S, Fe), the solar wind (Ar, Ne), solar active regions (Ne), and helioseismic data (He); abundances of non-volatile elements are also found from meteoritic data (Grevesse & Sauval 1998; Holweger 2001; Lodders 2003; Grevesse et al. 2007). Solar abundances from these studies are listed in Table 8. Our results, discussed below, indicate that if the LIC has a solar abundance composition, as indicated by the  $^{18}\text{O}$  and  $^{22}\text{Ne}$  data, then the lower abundances found by Grevesse et al. (2007) are preferred by our models.

**Ne:** In these models we have assumed the Ne abundance is 123 ppm (Anders & Grevesse 1989), which is based on a combination of photospheric and interstellar data. Solar system Ne abundances are difficult to measure because of FIP effects, however values include 77 ppm (Grevesse et al. 2007, after adding 0.05 dex to account for gravitational settling of the elements), and  $\sim 41$  ppm for solar wind in coronal holes (Gloeckler & Geiss 2007). The predicted densities of  $n(\text{Ne}^0)$  in the CHISM for models 26 and 28 (Table 4) are in agreement with the most recent PUI results for Ne (Table 1), and Ne densities as low as  $\sim 100$  ppm are allowed when filtration is included.

The CHISM Ne abundances indicated by these results appear to be consistent with Ne abundances and ionization levels in the global ISM. The Ne abundance in the Orion nebula is 100 ppm (Simpson et al. 2004). Takei et al. (2002) measured X-ray absorption edges formed by Ne and O in the interstellar gas and dust towards Cyg X-2, and found abundances of  $\text{Ne}/\text{H} \sim 92$  ppm and  $\text{O}/\text{H} \sim 579$  ppm when both atomic and compound forms in the sightline were included. Juett et al. (2006) observed the X-ray absorption edges of Ne and O towards nine X-ray binaries which sampled both neutral and ionized warm material, and found that the ionized states formed in the ionized material have the ratio  $\text{Ne III}/\text{Ne II} \sim 0.23$ . This value is identical to the predictions of model 26,  $\text{Ne III}/\text{Ne II} \sim 0.23$ , a fortuitous agreement that may indicate that the EUV radiation field in the CHISM is similar to the generic galactic EUV field in the solar vicinity.

**Ar:** Solar Ar abundance determinations range between  $\text{Ar}/\text{H} \sim 1.4 - 5.0$  ppm (Table 8); we have assumed  $\text{Ar}/\text{H} = 2.82$  ppm. The predicted Ar density at the Sun is within the uncertainties of the PUI data, although the range of possible filtration factors (0.64 – 0.95, see §2.2) also allow considerable leeway.

**O:** In the warm ISM such as the LIC, the ionization of oxygen and hydrogen is tightly coupled over timescales of  $\sim 100$  years by charge transfer (Field & Steigman 1971), so that the assumed  $N(\text{H I})$  combined with  $N(\text{O I})$  measurements act to constrain the deduced O abundance in the gas. The two best models (26, 28) correspond to  $\text{O}/\text{H} = 331$  ppm, however the O column density measurements are based on the saturated 1302Å line, and have  $\sim 35\%$  uncertainty. The modeled LIC value of  $\text{O}/\text{H} \sim 331$  ppm indicates that  $\sim 35\%$  of the O atoms are depleted onto dust grains. An oxygen filtration factor of  $f_{\text{O}} \sim 0.75$  is required by the PUI data and Model 26.

These models yield gas-phase O abundances that are consistent with observations of more distant interstellar sightlines. The ratio  $N(\text{O I})/N(\text{H I})$  is measured in both low and high extinction clouds. Oliveira et al. (2003) used unsaturated O I lines in the 910–1100Å interval and found  $\text{O I}/\text{H I} = 317 \pm 19$  ppm for  $\sim 30$  sightlines that included both types of material. Sightlines with detected  $\text{H}_2$ ,  $N(\text{H}) > 10^{20.5} \text{ cm}^{-2}$  and  $\langle n_{\text{H}} \rangle = 0.1 - 3.3 \text{ cm}^{-3}$ , yield  $\text{O}/\text{H} = 319 \pm 14$  ppm (Meyer et al. 1997). A survey of 19 stars with an average distance of 2.6 kpc by André et al. (2003) found  $\text{O I}/\text{H I} = 408 \pm 14$  ppm, where the long sightline and high average value  $N(\text{H})/E(B - V) = 6.3 \times 10^{21} \text{ cm}^{-2} \text{ mag}^{-1}$  indicate a bias towards sightlines containing many clouds that individually have low extinctions. A larger sample of 56 sightlines for a range of extinctions and distances show that sightlines with higher average mean densities,  $\langle n_{\text{H}} \rangle$ , show  $\text{O}/\text{H} = 284 \pm 12$  ppm, versus  $\text{O}/\text{H} = 390 \pm 10$  ppm for stars with low values of  $\langle n_{\text{H}} \rangle$  (Cartledge et al. 2004). For comparison, solar abundance studies yield a range of  $\sim 450 - 780$  ppm.

**C:** The best Models 26 and 28 yield a gas-phase abundance of C of  $\text{C}/\text{H} = 661$  and 708 compared to solar abundances of  $\sim 240 - 500$  ppm, which is consistent with our earlier results (Slavin & Frisch 2006) indicating an overabundance of C in the LIC. We speculate that shock destruction of carbonaceous grains, perhaps combined with some local spatial decoupling between carbonaceous and silicate grains, may explain these findings.

Singly-ionized carbon is an important coolant in the LIC (§5.5), so the C overabundance is required to maintain the temperature of the CHISM at the observed value. The carbon abundance obtained here indirectly depends on the  $\text{Mg II} \rightarrow \text{Mg I}$  dielectronic recombination coefficient that determines the ratio  $\text{Mg II}/\text{Mg I}$ , since that ratio is used as a criteria for the best models. The same ionization correction that gives the C abundance also successfully predicts Ne ionization in global WPIM and the S abundances in the LIC, although this may be a fortuitous coincidence. In the adjacent sightline towards Sirius the LIC has  $N(\text{C II})/N(\text{H I}) = 1,050$  ppm (Hebrard et al. 1999). An ionization correction of 300% is required to make this value consistent with solar abundances, and such a large ionization correction is not consistent with the ionization levels of  $X(\text{H}) \sim 20 - 26\%$  found here. In contrast, sightlines with cold ISM show C abundances on the order of  $135 \pm 46$  ppm (Sofia et al. 1997; Sembach et al. 2000).

**N:** The best models (26 and 28) find  $\text{N}/\text{H} = 46 - 47$  ppm, compared to solar values of  $\sim 57 - 110$  ppm. These results are consistent with the PUI results,  $\text{N}/\text{H} \sim 19 - 47$  ppm, after filtration factor uncertainties are included. The N and O results and favor an

ISM abundance pattern for volatiles similar to the Grevesse et al. (2007) photospheric abundances.

**S:** The best models predict S/H = 16–17, compared to solar values of  $\sim 13 - 27$  (including uncertainties, see Table 8). Sulfur is found to have little or no depletion onto dust grains in warm diffuse ISM (e.g. Welty et al. 1999).

**Mg, Si, Fe:** These refractory elements are observed in the LIC gas with abundances far below solar (factors of 3–15). Approximately 92%, 82%, and 77% of the Fe, Mg, and Si, respectively, are presumably depleted onto interstellar dust grains. If (Grevesse et al. 2007) abundances are assumed for the LIC, then to within the uncertainties the LIC dust has the relative composition of Fe:Mg:Si:O = 1:1:1:4, as is consistent with amorphous olivines  $\text{MgFeSiO}_4$ . Fe and Si are dominantly singly ionized, while Mg has a significant fraction ( $\sim 15\%$ ) that is twice ionized. The gas-phase abundances of these refractory elements are highly subsolar, even after ionization corrections are made, indicating that these elements are substantially depleted onto interstellar dust grains. In contrast to C, however, the silicate dust in the LIC that carries the missing Mg, Si, and Fe has experienced far less destruction than the carbonaceous grains.

**Ca II, Na I:** Weak lines of the trace ionization species Ca II and Na I are common diagnostics of ionization and abundance for interstellar clouds, including the partially ionized LIC; Na I is also frequently used as a diagnostic of the H column density. We note that our models show that the ratios  $N(\text{Ca II})/N(\text{Na I})$ ,  $N(\text{Na I})/N(\text{H})$ , and  $N(\text{Na I})/N(\text{H I})$  vary by 30%, 77%, and 93%, respectively, between the best models (Models 26–30, 42). As trace ionization species, the densities of Na I and Ca II are highly sensitive to volume density,  $n(\text{Na}^0)$ ,  $n(\text{Ca}^+) \propto n(\text{H})n_e$ . We therefore conclude that Na I and Ca II are imprecise diagnostics of ionization levels, H density, and abundances in warm partially ionized clouds.

#### 5.4. Gas-to-Dust Mass Ratio

Because the abundances are automatically corrected for unobserved  $\text{H}^+$ , we use the model results to infer the total mass of the interstellar dust, providing that the gas and dust in the LIC form a coupled and closed system that evolves together as the cloud moves through the LSR. The LIC LSR velocity is 16–21 pc/Myr, so that a LIC origin related to the Loop I or Scorpius-Centaurus superbubble would require that the LIC gas and dust remained a closed system over timescales of 4–5 Myr (Frisch & Slavin 2006; Frisch 1981). Gas-to-dust mass ratios calculated from the best models (26 and 28) using the missing-mass argument<sup>2</sup> are in the range  $R_{\text{G/D}} = 149 - 217$ , depending on solar abundances. The detailed information about  $R_{\text{G/D}}$  for different assumptions and the different models is listed in table 9.

For comparison,  $R_{\text{G/D}}$  determined from comparisons of *in situ* observations of interstellar dust inside of the solar system, compared to the gas densities of these models, yield  $R_{\text{G/D}} = 115 - 125$  (Table 9, Landgraf et al. 2000; Altobelli et al. 2004). The *in situ*  $R_{\text{G/D}}$  is an upper limit, since the smallest interstellar dust grains (radii  $\leq 0.15 \mu\text{m}$ ) with large charge-to-mass ratios (and thus small Larmor radii) are excluded from the heliosphere by the interstellar magnetic field which is draped over the heliosphere.

For all the models, the  $R_{\text{G/D}}$  determined from comparing *in situ* dust measurements with the CHISM gas mass flux is

<sup>2</sup> This argument assumes that the ISM reference abundances, in this case solar abundances, represent the sum of the atoms in the gas plus the dust (Frisch et al. 1999).

**Table 9.** Gas-to-Dust Mass Ratios from Models and In Situ Observations

Source	Model <sup>a</sup>						
	14	26	27	28	29	30	42
GS98	137	149	196	149	197	150	138
Lodders	158	174	238	174	239	175	160
Grevesse	194	217	321	217	323	218	196
In Situ	115	116	123	116	125	116	107

<sup>a</sup> The source of the comparison solar abundances is listed in column 1 (Table 8). The *in situ* dust flux is from Landgraf et al. (2000), corrected downwards by 20% as recommended by Altobelli et al. (2004) to account for side-wall impacts.

**Table 10.** Major Heat Sources in LIC Gas<sup>a</sup>

Source <sup>b</sup>	Fraction of Heating
H I	0.657
He I	0.248
dust	0.055
He II	0.016
cosmic rays	0.010

<sup>a</sup> Results for model 26. Other models are qualitatively the same, though there are some quantitative variations.

<sup>b</sup> For lines with ion names, the source here denotes the ion that is photoionized. Dust heating comes from photoelectric ejection by photons of the background FUV radiation field. Cosmic ray heating comes from electron impact ionization of the gas and direct heating of the electrons in the LIC plasma by the cosmic ray electrons.

lower than that determined by assuming solar abundances and using the gas phase abundances we determine to find  $R_{\text{G/D}}$ . This suggests that somehow the dust flowing into the heliosphere is concentrated relative to the gas, compared to the overall LIC sightline towards  $\epsilon$  CMa. The lower solar abundances of Grevesse et al. (2007) result in lower required depletions, and produces stronger disagreements with  $R_{\text{G/D}}$  determined from *in situ* data. We do not understand this result, which we have found previously (Frisch et al. 1999). Since  $R_{\text{G/D}}$  is sensitive to the mass of Fe in the dust grains (Frisch & Slavin 2003), we suggest that this difference may indicate inhomogeneous mixing of the gas and silicate dust over the  $\sim 0.64$  pc extent of the LIC.

#### 5.5. Heating and Cooling Rates

The heating and cooling rates for Model 26 are listed in Tables 10 and 11. The primary heat sources are photoelectrons from the ionization of  $\text{H}^0$  and  $\text{He}^0$ , with dust and cosmic ray heating contributing less than 7% of the heating. The dominant source of cooling is the [C II] 157.6  $\mu\text{m}$  fine-structure line, making up 43% of the total. This is more than twice the contribution of any other coolant. Nearly all the cooling is due to optical and infrared forbidden lines with many lines contributing at the  $\sim 1\%$  level. H recombination, free-free emission and dust, through the capture of electrons onto grain surfaces, also contribute at about a 2% level. The importance of C II as both a constraint on the C abundance in our models as well as a major coolant means that any model that aims to reduce the abundance of C to a solar level faces severe difficulties. The models with LIC temperatures in the  $T_{\text{He}^0} = 6300 \pm 340$  K range indicated by

**Table 11.** Major Coolants in LIC Gas<sup>a</sup>

Ion/Line	Fraction of Cooling
[C II] 157.6 $\mu\text{m}$	0.428
[S II] 6731 $\text{\AA}$	0.145
Fe II (total)	0.074
[Si II] 34.8 $\mu\text{m}$	0.065
[Ne II] 12.8 $\mu\text{m}$	0.035
[O I] 63.2 $\mu\text{m}$	0.028
H recomb.	0.024
dust	0.024
[Ne III] 15.6 $\mu\text{m}$	0.020
[N II] 6584 $\text{\AA}$	0.018
net free-free	0.018
[O I] 6300 $\text{\AA}$	0.017
[O II] 3727 $\text{\AA}$	0.011
[Ar II] 6.98 $\mu\text{m}$	0.011

<sup>a</sup> Results for model 26. Other models show similar results.

the *in situ* He<sup>0</sup> data all require supersolar abundances of C. The total heating/cooling rate for the LIC at the Sun for this model is  $3.55 \times 10^{-26}$  ergs cm<sup>-3</sup> s<sup>-1</sup>.

### 5.6. Radiation Field

Recently it has been proposed that a significant portion of the SXRb can be attributed to charge-transfer (a.k.a. charge exchange) between the solar wind ions (e.g., O<sup>+7</sup> and O<sup>+8</sup>) and interstellar neutrals (Cravens 2000; Snowden et al. 2004; Wargelin et al. 2004; Smith et al. 2005; Koutroumpa et al. 2006). While it seems at present that some fraction of the low energy X-rays are from this mechanism, it is unclear how large that fraction is. We note that basing the properties of the local hot plasma in the galactic plane on SXRb emission at energies  $E > 0.3$  keV is problematical. (Bellm & Vaillancourt 2005) have compared the Wisconsin B and Be band data with the ROSAT R12 data, and concluded that the observed anticorrelation between R12 and  $N(\text{H I})$  indicates that more than 34% of the SXRb generated in the Galactic disk must come from the Local Bubble. They also concluded that a heavily depleted plasma with  $\log T \sim 5.8$  is consistent both with the McCammon et al. (2002); Sanders et al. (2001) X-ray spectral data, and the upper limits set on the EUV emission by CHIPS (Hurwitz et al. 2004). When the Robertson & Cravens (2003) models of SXRb production by charge-transfer with the solar wind are considered, then only half of the SXRb in the plane is required to arise from a hot local plasma. We also note that the atomic physics for the calculation of the low energy part of the emission is still quite uncertain (V. Kharchenko, private communication). At this point we take the simple approach of ignoring the charge-transfer emission, though we plan to consider its possible impact in future work by reducing the assumed SXRb flux from hot gas. As noted previously, a lower SXRb flux due to a lower pressure in the hot gas does not necessarily have any impact on our calculated flux from the evaporative cloud boundary.

### 5.7. LIC Pressure

The strength of the interstellar magnetic field in the LIC is unknown, though modeling of its effects on the heliosphere sets some constraints. Our best models (26 and 28) presented here have a thermal pressure of  $\sim 2100$  cm<sup>-3</sup> K for the LIC. If the

thermal and magnetic pressures are equal, this indicates a magnetic field strength  $B \sim 2.7 \mu\text{G}$ , in agreement with field strengths for these models. As noted in §2.3, the main effect of the field strength in the models is to regulate the pressure in the evaporative cloud boundary, which in turn affects the flux of diffuse EUV radiation incident on the cloud. The amount of EUV flux helps determine the temperature in the cloud, which is how the observational constraints fix the magnetic field strength in the context of our modeling. Thus we do not explicitly fix the magnetic field strength with the goal of achieving equipartition and indeed some of our successful models have lower or higher field strengths. It is probably coincidental that the field strength required to match the *in situ* He<sup>0</sup> temperature for our best models is also close to the equipartition field strength, but it is at least encouraging that this field strength is consistent with our photoionization models. We note that if thermal, cosmic ray, and magnetic pressures are approximately equal the LIC has a pressure of  $\sim 6300$  cm<sup>-3</sup> K.

### 5.8. Comparisons with other LISM Sightlines

There have been a number of efforts to understand the LISM ionization and abundances (Frisch et al. 1986; Cheng & Bruhweiler 1990; Lallement & Bertin 1992; Vallerga 1996; Lallement & Ferlet 1997; Holberg et al. 1999; Kimura et al. 2003). The studies that attempt to derive gas phase elemental abundances find a range of results, generally fairly consistent with ours. A point of particular interest is the abundance of carbon that is surprisingly overabundant in our results. As an example, Kimura et al. (2003) find (based on four sightlines and excluding the  $\epsilon$  CMa and  $\beta$  CMa sightlines), a subsolar C abundance in contradiction with our results. Results for thirteen sightlines from Redfield & Linsky (2004) with velocity components consistent with the LIC velocity vector show that  $N(\text{C II})/N(\text{O I}) > 1$  for 8 of them, especially those at lower column density indicating a solar or supersolar C abundance. For our best models  $N(\text{C II})/N(\text{O I}) \approx 2$ . Our series of studies are unique in that we model the radiation field incident on the cloud, include radiative transfer effects, and calculate the thermal equilibrium within the cloud. The ionization varies through the cloud as does the temperature and density (slightly) and we compare observations within the heliosphere with the physical conditions at that point in the cloud rather than basing the model on line-of-sight averages.

Our present results indicate that  $n(\text{N II})/n(\text{N I}) \sim 0.32 - 0.50$  at the solar location, with N becoming more ionized as the sightline approaches the cloud surface. The column density ratio is thus higher, ranging from 0.38 - 0.62. Observed values of  $N(\text{N II})/N(\text{N I})$  toward other nearby stars are  $0.58^{+0.56}_{-0.77}$  toward Capella (Wood et al. 2002),  $1.29 \pm 0.23$  toward HZ43 (Kruk et al. 2002),  $1.91^{+0.87}_{-0.69}$  towards WD1634-573 (Lehner et al. 2003), and  $1.13 \pm 0.24$  towards  $\eta$  UMa (Frisch et al. in preparation). The total H I column density towards each of these stars is greater than the  $N(\text{H I}) \sim 4 \times 10^{17}$  cm<sup>-2</sup> found for the best models here. The nearest of these stars, Capella, has an ionization comparable to that of the LIC. The two high-latitude stars HZ43 and  $\eta$  UMa appear to sample low opacity regions where the ionization is larger than at the Sun, as does the WD1634-573 sightline that appears to cross the nearby diffuse H II region seen towards  $\lambda$  Sco (York 1983). As we have noted the  $\epsilon$  CMa line of sight is special because that star is the dominant source of stellar EUV photons for the LIC. Thus for sightlines at a large angle from the  $\epsilon$  CMa sightline, if the H I column between points along the sightline and  $\epsilon$  CMa is small the apparently high column points

are subject to a strong EUV field. Such geometry dependent ionization effects can be important for non-spherical clouds subject to a strongly spatially variable ionizing radiation source.

The variation in the fractional ionization of the CLIC gas has a direct impact on our understanding of the distribution and physical properties of low column density clouds for several reasons. (1) Abundances of elements with FIP < 13.6 eV must always be calculated with respect to  $N(\text{H I}) + N(\text{H II})$  for very low column density clouds. (2) Cloud geometry affects the opacity of observed sightlines so that the opacity to ionizing radiation is not directly traced by the observed value of  $N(\text{H I})$ . For lines of sight other than that towards  $\epsilon$  CMa, this could require more complex radiative transfer models in which the difference between the line of sight toward the star and that toward one of the primary sources of ionizing flux,  $\epsilon$  CMa, at each point is taken into account.

## 6. Conclusions

There are many uncertainties regarding the detailed properties of the ionizing interstellar radiation field incident on the LIC. The data we have on the LIC, both from absorption line studies and *in situ* measurements by spacecraft in the heliosphere, provide us with strong constraints on the ionization and composition of the LIC and particularly the CHISM. By exploring a range of models for the ISRF we find that while a fairly broad range of radiation fields can produce photoionization consistent with the data, other outputs from the models fall within a relatively narrow range of values. Our results for the models explored in this paper in which we require our models to be consistent with the LIC component of the absorption lines observed towards  $\epsilon$  CMa include:

1. For a range of assumptions regarding the H I column density of the LIC,  $N(\text{H I}) = (3.0 - 4.5) \times 10^{17} \text{ cm}^{-2}$ , and temperature of the hot gas of the Local Bubble,  $\log T_h = 5.9, 6.0$  and  $6.1$ , we are able to find model parameters that allow a match of the model results with best observed quantities,  $n(\text{He}^0)$ ,  $T(\text{He}^0)$  and  $N(\text{Mg II})/N(\text{Mg I})$ . For these models we assume that the cloud is evaporating because of thermal conduction between the hot Local Bubble gas and the warm LIC gas and include the emission from the cloud boundary.
2. For the best models in terms of fits to data, the required input parameters are: initial (i.e. at the outer edge of the cloud) total H density,  $n(\text{H}) \approx 0.21 - 0.23 \text{ cm}^{-3}$ ; and cloud magnetic field,  $B_0 \leq 3.8 \mu\text{G}$ .
3. If we assume that the magnetic field configuration reduces thermal conductivity at the boundary enough to prevent evaporation and ignore any radiation from the cloud boundary, we find that for most cases the radiation field does not cause sufficient heating to maintain the LIC at the temperature observed,  $T = 6,300 \pm 340 \text{ K}$ . One set of parameter choices, though, yields a successful model. These parameters are  $N(\text{H I}) = 4.5 \times 10^{17} \text{ cm}^{-2}$  and  $\log T_h = 6.1$ .
4. Despite the wide range of possible input parameters, the output values for quantities important for shaping the heliosphere are confined to a fairly small range:  $n(\text{H}^0) = 0.19 - 0.20 \text{ cm}^{-3}$ , and  $n_e = 0.05 - 0.08 \text{ cm}^{-3}$ .
5. A H filtration factor of  $f_H = 0.55 \pm 0.03$  yields good agreement between the radiative transfer model predictions for  $n(\text{H I})$  in the CHISM, and  $n(\text{H I})$  at the termination shock as found from observations of PUIs, the H I Ly $\alpha$  glow, and the solar wind slow-down in the outer heliosphere. This filtration value is also consistent with heliosphere models of the

ionization of interstellar H atoms traversing the heliosheath regions.

6. Elements with ionization potentials 13.6 – 25 eV, e.g. H, He, N, O, Ne, and Ar, are partially ionized with ionization fractions of  $\sim 0.2 - 0.7$ .
7. By requiring that the models match the column densities derived from absorption line data we are able to determine the necessary elemental abundances for several elements. We find that the abundances of N and O may be somewhat sub-solar. Sulfur is roughly solar, and C is substantially super-solar. Mg, Si and Fe are all sub-solar by factors of 3 – 15. The depletions of Fe, Mg, Si and O in the LIC are consistent with a dust population consisting of amorphous silicate olivines  $\text{MgFeSiO}_4$ , though other compositions for the dust are possible as well. We conclude that any carbonaceous dust in the LIC must have been destroyed, while silicate dust has persisted. Except for the gas-to-dust mass ratio, these results are in better agreement with the lower solar abundances of Grevesse et al. (2007). However we note that the O and Ne abundances of Lodders (2003) are in better agreement with other astronomical data such as the X-ray absorption edges.
8. The gas-to-dust mass ratio derived from missing mass in the gas-phase for our best models depends strongly on the assumed reference abundance set and range from 137 – 323. Our two best models, nos. 26 and 28, give a range of 149 – 217. For these same models  $R_{G/D} = 115 - 125$  based on the observed flux of dust into the heliosphere. The discrepancy of these values is minimized, in fact leading to consistency within the errors, if one assumes an abundance set such as that of GS98 which has large abundances of the metals. The GS98 abundances lead to substantial O depletion, however, which is not easily explained and conflict with the S abundances found for models 26 and 28.
9. These models also show that the densities of the trace ionization species Ca II and Na I are extremely sensitive to density and ionization. Therefore the ratios  $N(\text{Ca II})/N(\text{Na I})$ ,  $N(\text{Na I})/N(\text{H I})$ , and  $N(\text{Na I})/N(\text{H})$  are, by themselves, inadequate diagnostics of warm low density diffuse gas.

*Acknowledgements.* We would like to thank George Gloeckler for sharing data with us prior to publication, and Alan Cummings for pointing out that the ACR isotopic data indicate that the LIC abundances are solar. We also thank the International Space Science Institute in Bern, Switzerland for hosting the working group on “Interstellar Hydrogen in the Heliosphere.” This research was supported by NASA Solar and Heliospheric Program grants NNG05GD36G and NNG06GE33G to the University of Chicago, and by the NASA grant NNG05EC85C to SWRI.

## References

- Adams, T. F. & Frisch, P. C. 1977, *ApJ*, 212, 300  
 Ajello, J. M. 1978, *ApJ*, 222, 1068  
 Alibelli, N., Krüger, H., Moissl, R., Landgraf, M., & Grün, E. 2004, *Planet. Space Sci.*, 52, 1287  
 Altun, Z., Yumak, A., Badnell, N. R., Loch, S. D., & Pindzola, M. S. 2006, *A&A*, 447, 1165  
 Anders, E. & Grevesse, N. 1989, *Geochim. Cosmochim. Acta*, 53, 197  
 André, M. K., Oliveira, C. M., Howk, J. C., et al. 2003, *ApJ*, 591, 1000  
 Bellm, E. C. & Vaillancourt, J. E. 2005, *ApJ*, 622, 959  
 Bertaux, J. L. & Blamont, J. E. 1971, *A&A*, 11, 200  
 Bloch, J. J., Jahoda, K., Juda, M., et al. 1986, *ApJ*, 308, L59  
 Bzowski, M. 2003, *A&A*, 408, 1155  
 Bzowski, M., Gloeckler, G., Tarnopolski, S., Izmodenov, V., & Moebius, E. 2007, *A&A*, in press,  
 Cartledge, S. I. B., Lauroesch, J. T., Meyer, D. M., & Sofia, U. J. 2004, *ApJ*, 613, 1037  
 Cheng, K. & Bruhweiler, F. C. 1990, *ApJ*, 364, 573  
 Cowie, L. L. & McKee, C. F. 1977, *ApJ*, 211, 135  
 Cravens, T. E. 2000, *ApJ*, 532, L153

- Cummings, A. C., Stone, E. C., & Steenberg, C. D. 2002, *ApJ*, 578, 194
- Dupuis, J., Vennes, S., Bowyer, S., Pradhan, A. K., & Thejll, P. 1995, *ApJ*, 455, 574
- Ebel, D. S. 2000, *J. Geophys. Res.*, 105, 10363
- Egger, R. J. & Aschenbach, B. 1995, *A&A*, 294, L25
- Ferland, G. J., Korista, K. T., Verner, D. A., et al. 1998, *PASP*, 110, 761
- Field, G. B. & Steigman, G. 1971, *ApJ*, 166, 59
- Frisch, P. & York, D. G. 1986, in *The Galaxy and the Solar System* (University of Arizona Press), 83–100
- Frisch, P. C. 1981, *Nature*, 293, 377
- Frisch, P. C. 2007, “Composition of Matter”, *Space Sciences Series of ISSI*, publ. Springer, 27, 00
- Frisch, P. C., Dorschner, J. M., Geiss, J., et al. 1999, *ApJ*, 525, 492
- Frisch, P. C., Grodnicki, L., & Welty, D. E. 2002, *ApJ*, 574, 834
- Frisch, P. C. & Slavin, J. D. 2003, *ApJ*, 594, 844
- Frisch, P. C. & Slavin, J. D. 2005, *Advances in Space Research*, 35, 2048
- Frisch, P. C. & Slavin, J. D. 2006, *Short Term Variations in the Galactic Environment of the Sun, in it Solar Journey: The Significance of Our Galactic Environment for the Heliosphere and Earth*, Ed. P. Frisch (Springer), 133–193
- Frisch, P. C., York, D. G., & Fowler, J. R. 1986, in *ESA Special Publication*, Vol. 263, *New Insights in Astrophysics. Eight Years of UV Astronomy with IUE*, ed. E. J. Rolfe, 491–492
- Gloeckler, G. & Fisk, L. 2007, “Composition of Matter”, *Space Sciences Series of ISSI*, publ. Springer, 27, 00
- Gloeckler, G. & Geiss, J. 2004, *Advances in Space Research*, 34, 53
- Gloeckler, G. & Geiss, J. 2007, *A&A*, this volume
- Gloeckler, G. & Geiss, J. 2007, *Space Science Reviews*, 116
- Gondhalekar, P. M., Phillips, A. P., & Wilson, R. 1980, *A&A*, 85, 272
- Grevesse, N., Asplund, M., & Sauval, A. J. 2007, *Space Science Reviews*, 105
- Grevesse, N. & Sauval, A. J. 1998, *Space Science Reviews*, 85, 161
- Gry, C. & Jenkins, E. B. 2001, *A&A*, 367, 617
- Gurnett, D. A. & Kurth, W. S. 2005, *Science*, 309, 2025
- Hébrard, G., Mallouris, C., Ferlet, R., et al. 1999, *A&A*, 350, 643
- Hebrard, G., Mallouris, C., Ferlet, R., et al. 1999, *A&A*, 350, 643
- Henry, R. C. 2002, *ApJ*, 570, 697
- Holberg, J. B., Bruhweiler, F. C., Barstow, M. A., & Dobbie, P. D. 1999, *ApJ*, 517, 841
- Holweger, H. 2001, in *AIP Conf. Proc. 598: Joint SOHO/ACE workshop “Solar and Galactic Composition”*, 23–+
- Hurwitz, M., Sasseen, T. P., & Sirk, M. M. 2004, *ArXiv Astrophysics e-prints*
- Izmodenov, V., Malama, Y., Gloeckler, G., & Geiss, J. 2004, *A&A*, 414, L29
- Juett, A. M., Schulz, N. S., Chakrabarty, D., & Gorczyca, T. W. 2006, *ApJ*, 648, 1066
- Kimura, H., Mann, I., & Jessberger, E. K. 2003, *ApJ*, 582, 846
- Koutroumpa, D., Llallement, R., Kharchenko, V., et al. 2006, *A&A*, 460, 289
- Kruk, J. W., Howk, J. C., André, M., et al. 2002, *ApJS*, 140, 19
- Llallement, R. & Bertin, P. 1992, *A&A*, 266, 479
- Llallement, R., Bertin, P., Ferlet, R., Vidal-Madjar, A., & Bertaux, J. L. 1994, *A&A*, 286, 898
- Llallement, R. & Ferlet, R. 1997, *A&A*, 324, 1105
- Llallement, R., Vidal-Madjar, A., & Ferlet, R. 1986, *A&A*, 168, 225
- Llallement, R., Welsh, B. Y., Vergely, J. L., Crifo, F., & Sfeir, D. 2003, *A&A*, 411, 447
- Landgraf, M., Baggaley, W. J., Grün, E., Krüger, H., & Linkert, G. 2000, *J. Geophys. Res.*, 105, 10343
- Landsman, W. B., Henry, R. C., Moos, H. W., & Linsky, J. L. 1984, *ApJ*, 285, 801
- Lehner, N., Jenkins, E., Gry, C., et al. 2003, *ApJ*, 595, 858
- Leske, R. A. 2000, in *AIP Conf. Proc. 516: 26th International Cosmic Ray Conference, ICRC XXVI*, ed. B. L. Dingus, D. B. Kieda, & M. H. Salamon, 274–+
- Leske, R. A., Mewaldt, R. A., Christian, E. R., et al. 2000, in *AIP Conf. Proc. 528: Acceleration and Transport of Energetic Particles Observed in the Heliosphere*, ed. R. A. Mewaldt, J. R. Jokipii, M. A. Lee, E. Möbius, & T. H. Zurbuchen, 293–+
- Linsky, J. L. & Wood, B. E. 1996, *ApJ*, 463, 254
- Lodders, K. 2003, *ApJ*, 591, 1220
- Möbius, E., Bzowski, M., Chalov, S., et al. 2004, *A&A*, 426, 897
- Müller, H.-R., Florinski, V., Heerikhuisen, J., et al. 2007, *A&A*, in press, submitted
- Müller, H.-R. & Zank, G. P. 2004a, *J. Geophys. Res.*, 7104
- Müller, H.-R. & Zank, G. P. 2004b, *Journal of Geophysical Research (Space Physics)*, 7104
- Marschall, L. A. & Hobbs, L. M. 1972, *ApJ*, 173, 43
- McCammon, D., Almy, R., Apodaca, E., et al. 2002, *ApJ*, 576, 188
- McCammon, D., Burrows, D. N., Sanders, W. T., & Kraushaar, W. L. 1983, *ApJ*, 269, 107
- McClintock, W., Henry, R. C., Linsky, J. L., & Moos, H. W. 1978, *ApJ*, 225, 465
- McClintock, W., Linsky, J. L., Henry, R. C., & Moos, H. W. 1975, *ApJ*, 202, 733
- Meyer, D. M., Cardelli, J. A., & Sofia, U. J. 1997, *ApJ*, 490, L103
- Mitchell, J. J., Cairns, I. H., & Robinson, P. A. 2004, *Journal of Geophysical Research (Space Physics)*, 109, 6108
- Oliveira, C. M., Hébrard, G., Howk, J. C., et al. 2003, *ApJ*, 587, 235
- Parravano, A., Hollenbach, D. J., & McKee, C. F. 2003, *ApJ*, 584, 797
- Pryor, W., Gangopadhyay, P., Sandel, W., et al. 2007, *A&A*, in press
- Quémerais, E., Lallement, R., Bertaux, J.-L., et al. 2006a, *A&A*, 455, 1135
- Quémerais, E., Lallement, R., Ferron, S., et al. 2006b, *Journal of Geophysical Research (Space Physics)*, 111, 9114
- Raymond, J. C. & Smith, B. W. 1977, *ApJS*, 35, 419
- Redfield, S. & Linsky, J. L. 2004, *ApJ*, 602, 776
- Richardson, J. D., Liu, Y., Wang, C., & McComas, D. J. 2007, *A&A*, in press
- Richardson, J. D., Wang, C., & Burlaga, L. F. 2004, *Advances in Space Research*, 34, 150
- Ripken, H. W. & Fahr, H. J. 1983, *A&A*, 122, 181
- Robertson, I. P. & Cravens, T. E. 2003, *Journal of Geophysical Research (Space Physics)*, 108, 6
- Rucinski, D., Cummings, A. C., Gloeckler, G., et al. 1996, *Space Science Reviews*, 78, 73
- Sanders, W. T., Edgar, R. J., Kraushaar, W. L., McCammon, D., & Morgenthaler, J. P. 2001, *ApJ*, 554, 694
- Savage, B. D. & Sembach, K. R. 1996, *ApJ*, 470, 893
- Sembach, K. R., Howk, J. C., Ryans, R. S. I., & Keenan, F. P. 2000, *ApJ*, 528, 310
- Simpson, J. P., Rubin, R. H., Colgan, S. W. J., Erickson, E. F., & Haas, M. R. 2004, *ApJ*, 611, 338
- Slavin, J. D. 1989, *ApJ*, 346, 718
- Slavin, J. D. & Frisch, P. C. 2002, *ApJ*, 565, 364
- Slavin, J. D. & Frisch, P. C. 2006, *ApJ*, 651, L37
- Smith, R. K., Edgar, R. J., Plucinsky, P. P., et al. 2005, *ApJ*, 623, 225
- Snowden, S. L., Collier, M. R., & Kuntz, K. D. 2004, *ApJ*, 610, 1182
- Snowden, S. L., Cox, D. P., McCammon, D., & Sanders, W. T. 1990, *ApJ*, 354, 211
- Snowden, S. L., Egger, R., Finkbeiner, D. P., Freyberg, M. J., & Plucinsky, P. P. 1998, *ApJ*, 493, 715
- Snowden, S. L., Egger, R., Freyberg, M. J., et al. 1997, *ApJ*, 485, 125
- Snowden, S. L., McCammon, D., & Verter, F. 1993, *ApJ*, 409, L21
- Sofia, U. J., Cardelli, J. A., Guerin, K. P., & Meyer, D. M. 1997, *ApJ*, 482, L105
- Stokes, G. M. 1978, *ApJS*, 36, 115
- Takei, Y., Fujimoto, R., Mitsuda, K., & Onaka, T. 2002, *ApJ*, 581, 307
- Thomas, G. E. & Krassa, R. F. 1971, *A&A*, 11, 218
- Vallerga, J. 1996, *Space Sci. Rev.*, 78, 277
- Vallerga, J. 1998, *ApJ*, 497, 921
- Wargelin, B. J., Markevitch, M., Juda, M., et al. 2004, *ApJ*, 607, 596
- Weller, C. S. & Meier, R. R. 1981, *ApJ*, 246, 386
- Welty, D. E., Hobbs, L. M., Lauroesch, J. T., et al. 1999, *ApJS*, 124, 465
- Witte, M. 2004, *A&A*, 426, 835
- Witte, M., Banaszkiewicz, M., & Rosenbauer, H. 1996, *Space Science Reviews*, 78, 289
- Wood, B. E., Linsky, J. L., & Zank, G. P. 2000a, *ApJ*, 537, 304
- Wood, B. E., Linsky, J. L., & Zank, G. P. 2000b, *ApJ*, 537, 304
- Wood, B. E., Redfield, S., Linsky, J. L., Müller, H.-R., & Zank, G. P. 2005, *ApJS*, 159, 118
- Wood, B. E., Redfield, S., Linsky, J. L., & Sahu, M. S. 2002, *ApJ*, 581, 1168
- York, D. G. 1974, *ApJ*, 193, L127
- York, D. G. 1983, *ApJ*, 264, 172

## List of Objects

‘ $\epsilon$  CMa’ on page 2

‘Sirius’ on page 3